9

Research Article

Sven Ebel, Yonas Lebsir, Torgom Yezekyan, N. Asger Mortensen and Sergii Morozov*

An atlas of photonic and plasmonic materials for cathodoluminescence microscopy

https://doi.org/10.1515/nanoph-2025-0135 Received March 20, 2025; accepted June 24, 2025; published online July 3, 2025

Abstract: Cathodoluminescence (CL) microscopy has emerged as a powerful tool for investigating the optical properties of materials at the nanoscale, offering unique insights into the behavior of photonic and plasmonic materials under electron excitation. We introduce an atlas of bulk CL spectra and intensity for a broad range of materials used in photonics and plasmonics. Through a combination of experimental CL microscopy and Monte Carlo simulations, we characterize spectra and intensity of coherent and incoherent CL, electron penetration depth and energy deposition, offering a foundational reference for interpreting CL signals and understanding material behavior under electron excitation. Our atlas captures CL signals across a wide range of materials, offering valuable insight into intrinsic emission properties for informed material selection and device design in photonics and plasmonics.

Keywords: cathodoluminescence; electron microscopy; photonics; plasmonics; Monte Carlo methods; angular emission profile

E-mail: semo@mci.sdu.dk. https://orcid.org/0000-0002-5415-326X

Sven Ebel, Yonas Lebsir and Torgom Yezekyan, POLIMA – Center for Polariton-Driven Light–Matter Interactions, University of Southern Denmark, Campusvej 55, DK-5230 Odense M, Denmark.

https://orcid.org/0009-0005-3224-6413 (S. Ebel).

https://orcid.org/0000-0002-9383-0278 (Y. Lebsir).

https://orcid.org/0000-0003-2019-2225 (T. Yezekyan)

N. Asger Mortensen, POLIMA – Center for Polariton-Driven Light–Matter Interactions, University of Southern Denmark, Campusvej 55, DK-5230 Odense M, Denmark; and Danish Institute for Advanced Study, University of Southern Denmark, Campusvej 55, DK-5230 Odense M, Denmark. https://orcid.org/0000-0001-7936-6264

1 Introduction

Cathodoluminescence (CL) microscopy is an indispensable tool for investigating the optical and electronic properties of materials at the nanoscale, providing valuable insights into photonic and plasmonic materials [1]–[5]. When an electron beam interacts with a material, it can generate a broad range of emissions, including X-rays, secondary and backscattered electrons, and photons spanning from the ultraviolet (UV) to the infrared (IR) spectral range. Among these, UV to IR photons are of particular interest for photonics and plasmonics.

The detection of CL optical signal combined with the techniques of electron microscopy allows for the spatial mapping of the material's electronic and optical characteristics with nanoscale resolution, overcoming the constraints faced by photoluminescence (PL) microscopy, which is limited by optical diffraction and governed by optical selection rules [6]. In contrast, CL microscopy directly excites electronic states, revealing intrinsic material properties at nanoscale. The wavelength and intensity of the emitted light under electron beam excitation are influenced by the material's composition, defects, and structural features, making CL microscopy particularly valuable for comprehensive characterization. For in-depth insights into various aspects of CL, readers are directed to several extensive reviews, which include discussions on the physical fundamentals of CL [6], [7], its historical development and methods [2]-[4], [8]-[12], overviews on CL origin in a variety of semiconductors [1], [13], [14], and developments on CL microscopy for the study of photonic and plasmonic systems [5], [15], [16].

In combination with far-field Fourier spectroscopy, CL microscopy offers a powerful method for distinguishing between coherent and incoherent light emission processes in materials [17]–[21]. Coherent CL arises from transition radiation, Smith–Purcell radiation, and collective oscillations of free electrons, such as surface-plasmon resonances in metals, while incoherent CL results from intrinsic processes (e.g., electron–hole recombination, defects) and extrinsic processes (e.g., dopants, impurity and color centers), which are typically observed in semiconductors and

^{*}Corresponding author: Sergii Morozov, POLIMA – Center for Polariton-Driven Light-Matter Interactions, University of Southern Denmark, Campusvej 55, DK-5230 Odense M, Denmark,

dielectrics [18], [22]. Differentiating and accurately attributing these mechanisms is important in photonic and plasmonic systems, as they often involve materials that support both processes. The relative strength of incoherent and coherent mechanisms strongly depends on the system's material composition. Therefore, for effective experiment design and interpretation, it is essential to understand the CL response of the materials used, independent of geometric effects, and to identify the origins of the observed spectral features.

An important parameter in CL microscopy is the electron penetration depth, which refers to how deeply the electron beam penetrates the material before losing its kinetic energy. The penetration depth varies depending on the material's atomic number (Z), atom density, and the energy of electrons in the electron beam [23]. For low-Z materials like carbon (C) or silicon (Si), penetration depths can be relatively large (on scale of microns), allowing for bulk material analysis even at lower electron beam voltages. Conversely, in high-Z materials like gold (Au) or platinum (Pt), the penetration depth is significantly reduced (down to sub 10 nm), restricting the interaction volume to the surface or near-surface layers. Understanding the electron penetration depth is relevant for interpreting CL accurately, as it determines whether the emission originates from the surface, subsurface, or bulk of the material [24]-[26]. The penetration depth and corresponding distribution of absorbed energy plays a key role in electron beam lithography, where precise energy deposition is essential for controlling pattern resolution and resist exposure [23].

In this article, we present a comprehensive study of the optical response from a wide range of materials under low-energy electron beam excitation (1-30 keV) in a scanning electron microscope (SEM), building up an atlas of CL spectra of materials for photonic and plasmonic systems. The materials studied include plasmonic and nonplasmonic metals, dielectrics, and semiconductors used in optics and photonics, as well as novel two-dimensional (2D) materials, topological insulators, and polymeric and resist materials used in the fabrication of nanostructured devices. Our aim is to probe the CL emission mechanisms (coherent/incoherent) and to characterize the emitted spectra and CL intensity from each material. We also perform numerical simulations of electron penetration depth and energy absorption using Monte Carlo methods via CASINO modeling tool [23]. These simulations provide detailed insights into the interaction of low-energy electrons with the investigated materials. Our work combines experimental CL analysis with Monte Carlo simulations, offering a robust dataset to

understand the impact of material properties and electron interactions on CL behavior. Furthermore, this atlas serves as a reference for interpreting CL data in various experimental contexts, reducing the likelihood of misinterpretation of emission origins, material properties, or electronmatter interactions. By systematically documenting the CL characteristics of key materials, this work facilitates the development of next-generation photonic and plasmonic technologies, guiding both experimental design and theoretical modeling efforts.

2 Materials

We present CL properties of a diverse range of commercially available materials (Figure 1), which serve as potential building blocks and platforms for emerging photonic and plasmonic devices. Each material is examined using low-energy (1–30 keV) and low current (ca. 1.4 nA) electron beams, allowing us to characterize the origin of CL emissions - whether coherent or incoherent - and analyze their spectra and intensity. Furthermore, the Supplementary Materials (SM) provide detailed information on the investigated materials, including their suppliers and origins, Raman spectra, and morphological characterization using optical and electron-based imaging techniques, as well as simulation results of electron beam interaction with the materials.

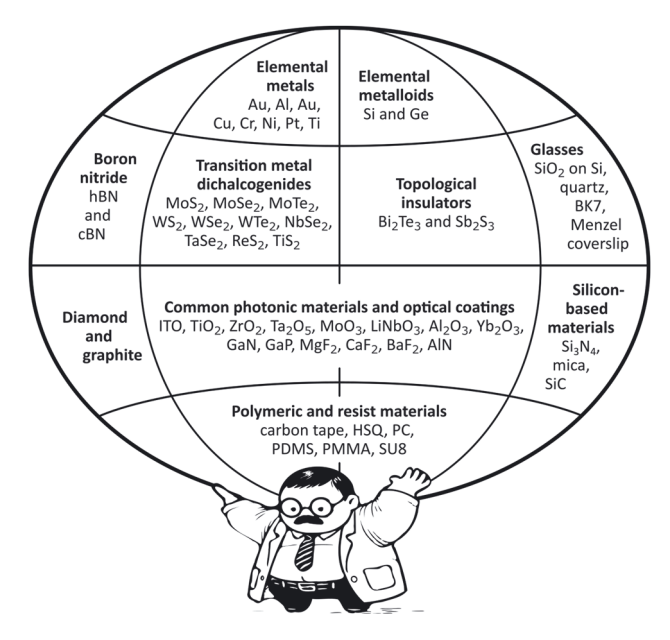


Figure 1: An atlas of investigated photonic and plasmonic materials.

3 Monte Carlo simulations

use Monte Carlo simulations performed with CASINO v2.42 [23] to model electron trajectories and the distribution of absorbed energy in various bulk materials under electron-beam excitation. CASINO software employs stochastic methods to simulate multiple electron scattering events, energy loss mechanisms, and backscattering, providing a spatial map of electron trajectories for primary electron (PE) and backscattered electrons (BSE). CASINO simulates elastic scattering and approximates inelastic events using the mean energy loss between successive elastic scattering interactions [27], [28]. All our simulations utilize interpolation from the Mott cross-section database [29], while the Joy-Luo stopping power model [30] is applied to account for ionization potential, collisions, and inelastic energy loss [27]. For a more in-depth discussion on the theory of free electron-matter interactions, which underpin the Monte Carlo simulations used in our work, we refer the reader to the books by Reimer [31] and Egerton [32].

We begin by presenting simulation results in Figure 2 on electron beam interaction with silicon (Si), exploring how varying electron beam energy influences electron propagation and energy deposition. Figure 2a presents the PE trajectory maps at 1 keV. In total, we simulate 10⁶ electrons, though only 50 trajectories are shown here for clarity. Figure 2b shows the corresponding statistics for the maximum penetration depth d_{PE} – defined as the point where electron energy falls below 0.1 keV. Higher electron beam energy results in deeper PE distributions, as shown in Figure 2c. We quantify these results by calculating the weighted mean of PE depth $\langle d_{PE} \rangle = \sum p_i d_{PE,i}$ where p_i represents the normalized probabilities, and two standard deviations, as illustrated in Figure 2b. Figure 2d summarizes the obtained $\langle d_{\rm PE} \rangle$ in Si over the electron beam energy range of 1–30 keV. As the electron beam energy increases, $\langle d_{pp} \rangle$ extends deeper into Si, from approximately 16 nm at 1 keV to nearly 5 µm at 30 keV. We compare these results to the Kanaya-Okayama range D_{pp} , which provides an estimate of how deep an electron can travel in a material before being fully absorbed, primarily considering energy loss due

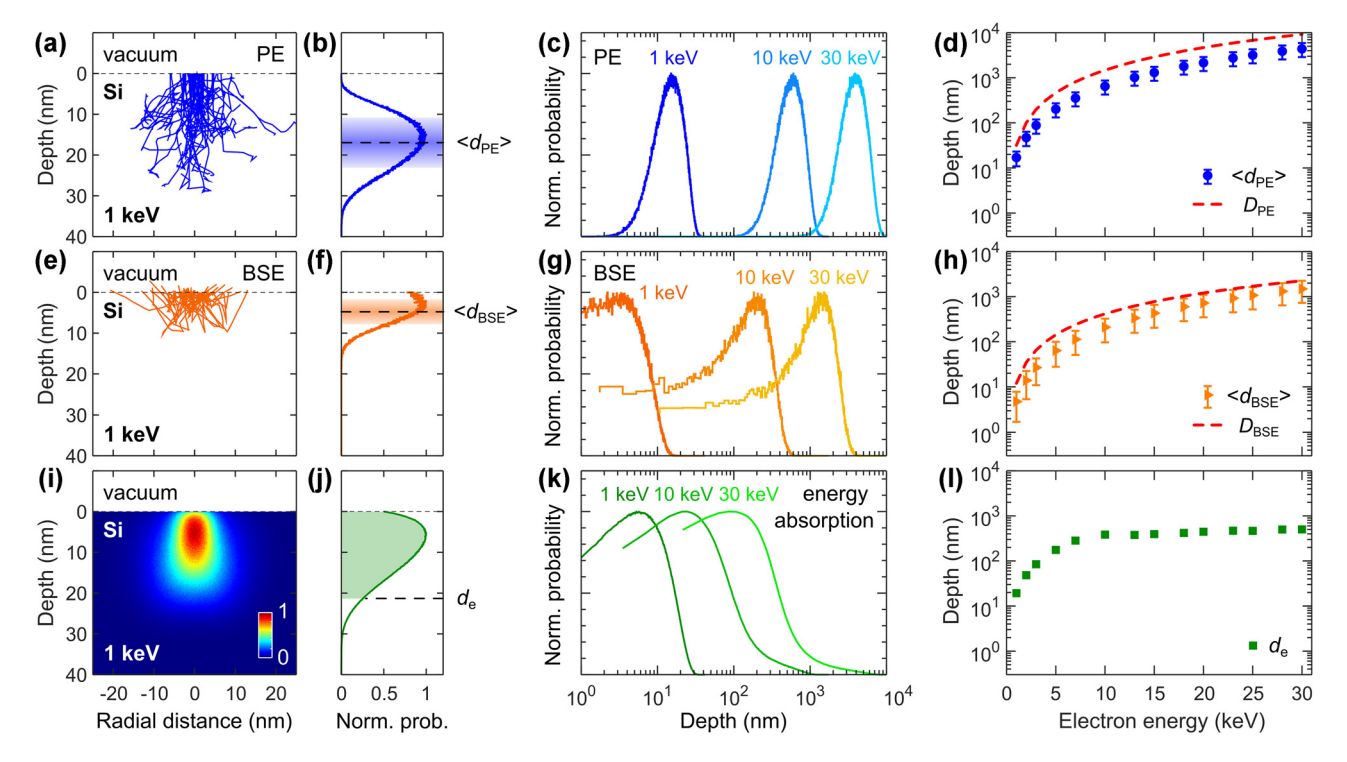


Figure 2: Monte Carlo simulations of electron trajectories and energy deposition in bulk Si at increasing electron beam energy. (a, e) PE and BSE trajectories for an incident electron beam at 1 keV with 10 nm diameter (shown only 50 trajectories). Corresponding distributions of the PE (b) and BSE (f) depth at 1 keV (acquired for 10^6 incident electrons). The horizontal dashed lines represent the weighted mean $\langle d_{\rm PE} \rangle$ and $\langle d_{\rm BSE} \rangle$, while the shaded areas show two standard deviations. Distributions of the PE (c) and BSE (g) depth at increasing electron beam energy (acquired for 10^6 incident electrons). (d, h) Increase of $\langle d_{\rm PE} \rangle$ and $\langle d_{\rm BSE} \rangle$ with electron energy. The error bars represent two standard deviations as shown in the corresponding panels (b) and (f). The dashed red lines are the Kanaya–Okayama range $D_{\rm PE}$ for PE in (d), and BSE origin depth $D_{\rm BSE}$ in (h). (i) Energy deposition map at 1 keV. (j) Axial profile of the energy deposition map from panel (i). The dashed line indicates the 90 % energy loss depth $d_{\rm e}$. (k) Axial profiles of the energy deposition at increasing electron beam energy. (l) Increase of $d_{\rm e}$ with electron beam energy.

to inelastic scattering [33]. The range is given by $D_{\rm PE}$ [nm] = $27.61 \cdot 10^{-5} A \cdot E^{5/3}/(\rho \cdot Z^{8/9})$, where 27.61 is a dimensional consistency factor, A is the atomic weight in g/mol, E is the electron energy in eV, ρ is the material density in g/cm³, and Z is the material's atomic number. We plot $D_{\rm PE}$ as a red dashed line alongside the Monte Carlo simulation results for $\langle d_{\rm PE} \rangle$ in Figure 2d. We note that the PE penetration depth increases with electron energy, following a power law trend.

In CASINO simulations, BSEs are defined as PEs that escape the sample surface after multiple scattering events, provided their energy remains above 0.1 keV upon exiting the material. Figure 2e presents the BSE trajectory maps in Si at 1 keV, and Figure 2f shows the corresponding statistics for the BSE origin depth d_{RSE} , which is defined as the depth of the first large-angle elastic scattering event (greater than 90° deflection) that initiates the trajectory leading the electron back to the surface. Higher electron beam energy results in deeper BSE origin depth distribution, as shown in Figure 2g. Similarly to PE, we characterize the BSE origin depth with weighted mean $\langle d_{\rm BSE} \rangle$ and two standard deviations, as illustrated in Figure 2f. Figure 2h summarizes the obtained $\langle d_{\text{RSE}} \rangle$ in Si over the electron beam energy range of 1–30 keV. $\langle d_{\rm BSE} \rangle$ increases in Si with electron energy from about 5 nm at 1 keV to 1.5 µm at 30 keV. We compare these results with experimental observations of BSE range

[31], [34], which is described by the empirical expression $D_{\rm BSE}$ [nm] = $28 \cdot E^{1.54}/\rho$, where 28 is an experimental scaling factor, E is the electron energy in keV, and ρ is the material density in g/cm³. We plot $D_{\rm BSE}$ as a red dashed line alongside the Monte Carlo simulation results for $\langle d_{\rm BSE} \rangle$ in Figure 2h, observing a power law trend.

We also investigate the impact of increasing electron beam energy on the spatial distribution of absorbed energy, as it is relevant for determining the origin of the CL signal. Figure 2i shows the spatial profile of electron energy deposition in Si at 1 keV, with the total energy summed for each depth in Figure 2j. We extract the depth d_e at which incident electrons lose 90 % of their energy from the energy deposition profile, as illustrated in Figure 2j. Furthermore, Figure 2k presents the evolution of energy absorption distributions for 1 keV, 10 keV, and 30 keV. Figure 2l summarizes the increase of $d_{\rm p}$ in Si with electron beam energy. Understanding the absorbed energy profiles helps in determining the effective electron-matter interaction volume, which is crucial for designing of CL experiments, CL characterization of photonic and plasmonic devices, and optimizing electronbeam lithography processes.

Taking a broader perspective, Figure 3 investigates how material density affects the characteristic depths $\langle d_{\rm PE} \rangle$, $\langle d_{\rm BSE} \rangle$ and $d_{\rm e}$. Figure 3a–c illustrate the reduction

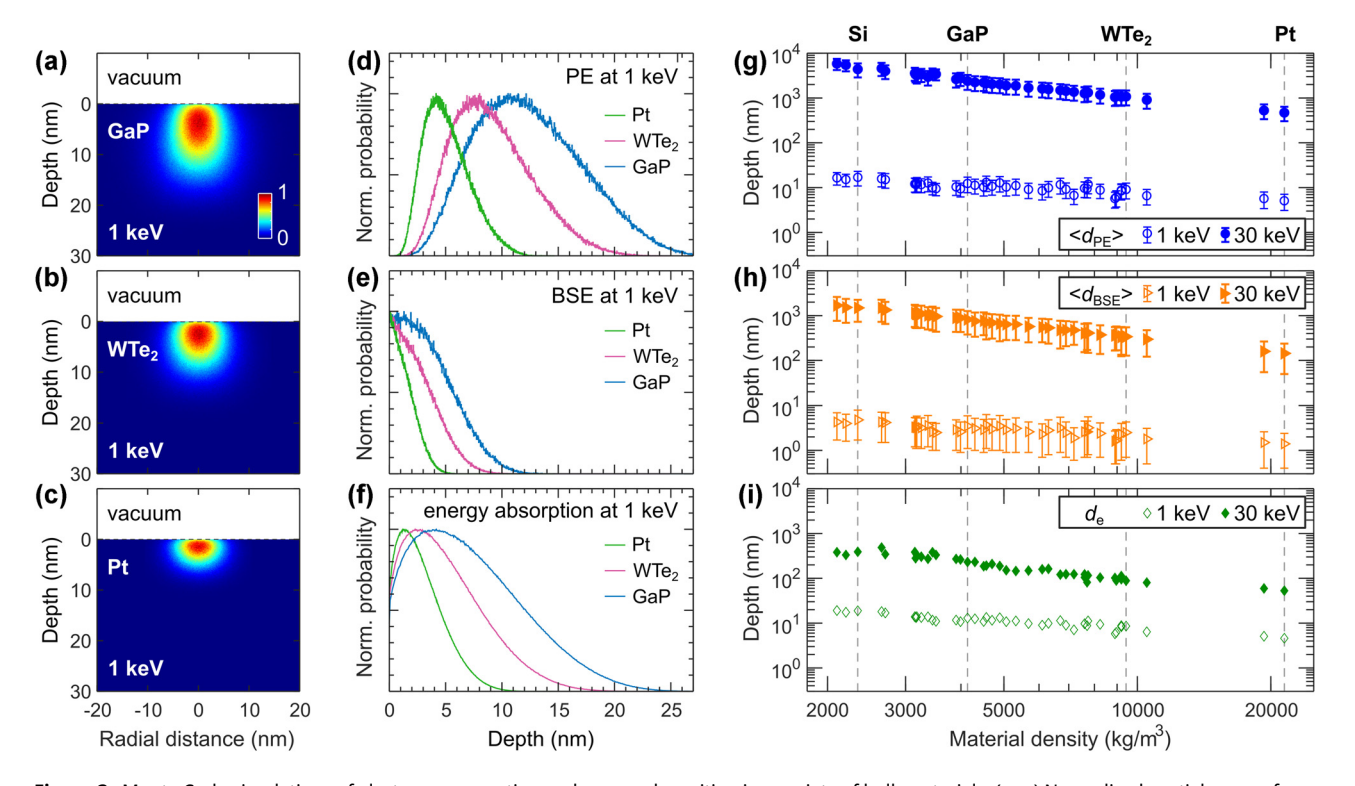


Figure 3: Monte Carlo simulations of electron propagation and energy deposition in a variety of bulk materials. (a–c) Normalized spatial maps of 1 keV electron beam energy deposition in GaP, WTe₂, and Pt. (d–f) 1 keV distributions of $d_{\rm PE}$, $d_{\rm BSE}$, and axial profiles of the absorbed power in GaP, WTe₂ and Pt. (g–i) Decrease of $d_{\rm PE}$, $d_{\rm BSE}$, and $d_{\rm e}$ for denser bulk materials at 1 keV (open symbols) and 30 keV (filled symbols). Densities of Si, GaP, WTe₂, and Pt are highlighted with vertical dashed lines. The error bars represent two standard deviations.

in electron–matter interaction volume as material density increases. To highlight these effects, we selected gallium phosphide (GaP, $\rho=4,138~{\rm kg/m^3}$), tungsten ditelluride (WTe₂, $\rho=9,430~{\rm kg/m^3}$), and platinum (Pt, $\rho=21,450~{\rm kg/m^3}$) for their distinctive densities. This selection emphasizes the differences in characteristic depth distributions of PE, BSE, and energy absorption at 1 keV, as shown in Figure 3d–f. We repeat these simulations for a wide range of materials with densities spanning from 2,100 kg/m³ for boron nitride (BN) to 21,450 kg/m³ for Pt and plot the characteristic depths at 1 keV and 30 keV in Figure 3g–i. The general trend indicates that characteristic electron depths decrease as material density increases. This effect is more pronounced at the higher electron beam energy of 30 keV (note the steeper slope for filled symbol dataset in Figure 3g–i).

Finally, Figure 4 summarizes the results of Monte Carlo simulations for backscattering coefficient β , which is the ratio of BSE to incident PE and provides an estimate of the electrons involved in inelastic interactions responsible for generating CL. A higher backscattering coefficient reduces the effective beam current available for generating CL, making it an important factor in evaluating CL efficiency. Interestingly, Figure 4 demonstrates that β is higher for lowdensity materials like Si at low electron beam energy of 1 keV, while the trend reverses for high-density materials like Pt. This result has been previously observed experimentally as a consequence of the interplay between elastic and inelastic scattering, where low-energy electrons in low-density materials penetrate deeper with less scattering, leading to higher β , while high-density materials exhibit stronger elastic scattering at higher energies, increasing β [35]. For reference, we provide a detailed listing in the SM of $\langle d_{\rm PE} \rangle$, $\langle d_{\rm RSE} \rangle$, $d_{\rm e}$, and β for all the investigated materials.

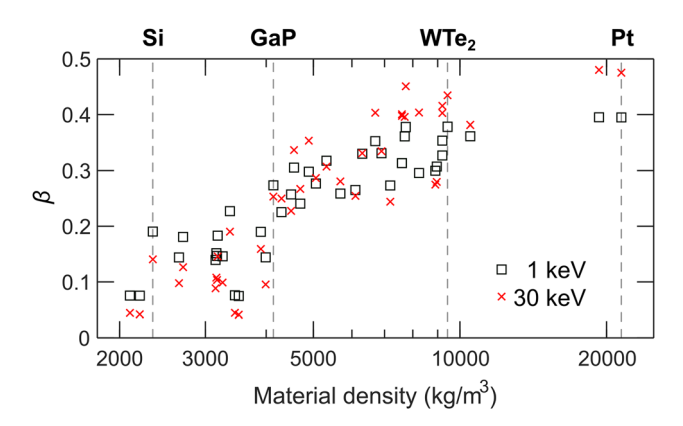


Figure 4: Monte Carlo simulations of backscattering coefficient β in bulk materials. Increase of β with material density at 1 keV (squares) and 30 keV (crosses). Densities of the selected materials are indicated by vertical dashed lines.

Having modeled electron—material interactions through Monte Carlo simulations, we gained detailed insight into how electron beam energy and material properties influence penetration depth, energy deposition, and backscattering behavior. Low electron beam energies primarily excite near-surface regions, while high energies penetrate deeper, exciting a larger volume; in low-density materials, excitation occurs gradually over greater depths, whereas in high-density materials, energy is deposited closer to the surface due to stronger scattering. Building on these simulation results, the following sections outline the experimental procedures used to acquire and interpret CL emission data.

4 Experimental methods

4.1 Experimental setup

The experimental setup for CL microscopy (SPARC Spectral, Delmic) involves a scanning-electron microscope (SEM, TES-CAN MIRA3) equipped with a parabolic mirror (effective NA = 0.97) to collect the generated emission (Figure 5a). The electron beam passes through a small aperture in the parabolic mirror, interacting with the sample in its focal spot. The generated CL is collected by the same mirror and directed towards a spectrometer (Kymera-193i with Newton 920P, Andor). Our CL spectral measurements were performed at room temperature using a $1 \times 1 \mu m^2$ spot size with fuzzing (scanning within the pixel during signal acquisition); the integration time was adjusted based on the brightness of the CL signal, and dark counts were subtracted from all spectra. For angular-resolved measurements, a set of interchangeable lenses is used to image the Fourier plane, enabling the retrieval of angular radiation profiles and providing insight into the coherent or incoherent origin of the CL signal [17], [18].

4.2 Angular emission

Due to the uncorrelated nature of incoherent CL processes (Figure 5b), the emitted light has an isotropic or Lambertian emission profile, where the intensity is uniform across all directions and decreases with the cosine of the emission angle (Figure 5c). In contrast, the coherent CL originates from ordered, collective oscillations of electrons (Figure 5d). These coherent processes result in a dipolar emission pattern, where the intensity is strongest along the interface, typically aligned with the orientation of the dipole or the surface-plasmon mode. This angular dependence is due to the phase coherence of the emitted light, which causes

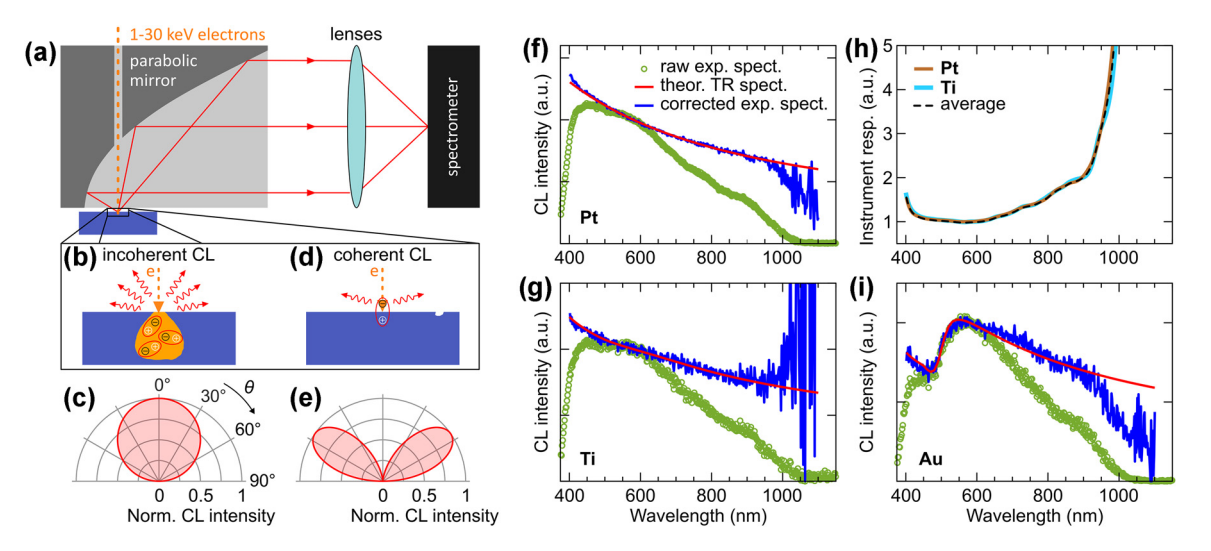


Figure 5: Cathodoluminescence microscopy. (a) Experimental setup for detection of CL emission and angular spectra. (b) Incoherent CL originates from the recombination of electron-hole pairs generated by incident electrons in the bulk and is characterized by an isotropic angular radiation pattern (c). (d) Coherent CL arises from the interaction of an electron beam with collective electron oscillations, as for example transition radiation (TR), and is characterized by a dipolar emission pattern (e). (f-g) Experimental TR spectra of Pt and Ti at 30 keV (green circles) are used to calibrate instrument response by comparing them with theoretical TR spectra (red), and obtaining the corrected CL spectra (blue, see main text for details). (h) Instrument response functions obtained with TR of Pt (brown) and Ti (cyan), and their average (dashed black). (i) The averaged instrument response function is applied to the experimental CL spectrum of gold at 30 keV (green circles), producing a corrected spectrum (blue), that closely matches the theoretical TR spectrum of gold (red).

constructive interference in specific directions, resulting in a non-uniform emission profile. Due to the presence of the interface between vacuum and sample, the intensity $I(\theta)$ of the dipolar emission pattern is bent towards the normal to interface, and can be modeled as $I(\theta) \propto \sin^2(\theta) \cos(\theta)$ (Figure 5e), where θ is an angle from the normal (see Figure 5c). We note that all reported experimental angular radiation profiles are collected within a θ range of 7° – 78° , with a dip around $\theta = 0^{\circ}$ caused by the central hole in the parabolic mirror for the electron beam, and truncation at large angles due to the mirror's limited numerical aperture.

The angular radiation pattern of CL provides insight into the specific radiation mechanism responsible for the emitted light. Furthermore, the intensity of coherent CL is strongly dependent on the electron beam energy and is generally dimmer compared to its incoherent counterpart [18]. In addition, coherent CL is broadband, whereas incoherent CL can exhibit very narrow emission lines, even at room temperature, as seen in color centers in diamonds [36]. We also observe that certain materials exhibit either coherent or incoherent CL, whereas others display a mixture of both or can transition from incoherent to coherent CL as the electron beam energy increases.

4.3 Instrument response

In CL spectroscopy, accurate broadband spectral measurements require correction for the instrument's response function, which accounts for wavelength-dependent variations in detection efficiency [18]. Several factors can introduce spectral distortions in our measurements. The spectrometer grating used (150 lines/mm, 500 nm blaze) has its highest diffraction efficiency around 500-600 nm, meaning wavelengths outside this range may be underrepresented. Additionally, the silicon-based photodetector exhibits a significant drop in sensitivity below ca. 400 nm and beyond 950 nm, affecting signal strength in these spectral regions. Optical components in the CL system, such as the fused silica SEM window and focusing optics, have spectrally dependent transmittance, introducing further variations across the detection range.

To account for these potential distortions and ensure reliable spectral measurements, we apply an instrument response correction, which is particularly crucial for broadband emission sources like transition radiation. Ensuring accurate spectral calibration allows for a meaningful comparison between experimental data and theoretical models, which predict transition radiation based on the material's optical properties and the electron beam parameters. In our study, transition radiation is modeled using the formalism described in prior work by García de Abajo [6], where Maxwell's equations are solved for a fast electron interacting with a material, inducing surface currents that generate a characteristic transition radiation spectrum (see details in SM). This modeling approach incorporates ellipsometry data to determine the dielectric function of the investigated materials, ensuring accurate spectral predictions.

To implement the instrument response correction, we first measure CL spectra of platinum (Pt) and titanium (Ti), as these metals exhibit well-characterized and uniform transition radiation. We use two metals to measure the instrument response in order to account for metalspecific variations in transition radiation emission. Moreover, to minimize geometry-related spectral contribution, experimental CL spectra of Pt and Ti are averaged over multiple positions on the samples. These experimental CL spectra for Pt and Ti at 30 keV are shown in Figure 5f and g (green circles) along with their theoretical transition radiation spectra (red curves). For calculating the theoretical spectra, we employ ellipsometry data for Pt and Ti from different experimental groups [37], [38], which helps to further average our instrument response results. By comparing the experimental spectra with the theoretical ones, we extract instrument response functions for each metal (brown for Pt and cyan for Ti in Figure 5h). Here we smoothed the experimental CL spectra for the calculation of the instrument response functions, ensuring a more representative and uniform spectral correction. We average the two response functions to minimize material-specific variations and systematic errors (dashed black in Figure 5h). As expected, the instrument response remains flat in the 500-600 nm range, where the grating achieves its highest diffraction efficiency, but sharply diverges beyond 900 nm, resulting from the poor detection efficiency of the silicon-based CCD camera in that region. Finally, in Figure 5f and g this averaged instrument response is applied to the raw CL spectra of Pt and Ti (green circles), resulting in the corrected CL spectra (blue).

We validate independently the obtained instrument response function using CL of gold (Au), as it has a well-characterized spectrum [18]. Figure 5i presents the experimental spectrum of Au at 30 keV (green circles) along-side the theoretical transition radiation spectrum (red), calculated using ellipsometry data from Ref. [39]. The corrected spectrum (blue) is obtained by applying the instrument response function, showing excellent agreement with the theoretical spectrum and accurately reconstructing spectral features in the 400–600 nm range, attributed to distinct variations in the real and imaginary parts of the

Au dielectric function, which influence the transition radiation intensity and spectral shape. As expected, the correction becomes unreliable beyond ca. 950 nm due to the low sensitivity of the silicon detector. Consequently, we report corrected spectra within the 400-950 nm range in our CL atlas, while raw spectra covering 400-1,100 nm are provided in SM Figures S1-S10. This process ensures that the spectral shape and intensity accurately reflect the intrinsic CL response of the materials reported in our atlas, eliminating distortions introduced by the CL detection system. Furthermore, another common source of distortion is the second-order diffraction artifact, which arises when bright emission sources produce unwanted spectral contributions at twice their fundamental wavelength. To mitigate this effect for materials with bright peaks in the UV region, we used a 450 nm long-pass filter and report CL spectra up to 900 nm.

5 Cathodoluminescence spectra

In this section, we present CL spectra obtained at electron beam voltages from 1 keV to 30 keV, demonstrating the effects of different voltages on various photonic and plasmonic materials. Lower beam voltages (\leq 5 kV) probe near-surface regions, revealing surface states and possible contaminants, while higher voltages (30 kV) penetrate deeper, uncovering bulk material response (Figures 2 and 3). This systematic reporting of CL spectra across a range of voltages helps to select appropriate experimental conditions, including background-free substrates for the desired spectral range and optimized beam energy for specific emission characteristics, aiding CL analysis in material science and nanotechnology.

5.1 Elemental metals

CL studies of elemental metals began gaining attention in the mid-20th century, focusing on the optical and electronic properties of metals under electron beam excitation. Metals like gold (Au), silver (Ag), copper (Cu), and aluminum (Al) were studied to explore their potential luminescence properties despite their free electron nature, primarily to elucidate the mechanism of transition radiation [40]–[43]. The 1980s saw a significant increase in interest, particularly due to advancements in CL spectroscopy, which allowed for the study of metal-semiconductor interfaces and the identification of related interface states [8], [44]–[46]. CL emission from metals could reveal unique interactions between conduction band electrons and *d*-band holes [47], Mie

resonances in metallic spheres [48], as well as surface plasmon effects [47], [49]–[59]. Today, CL methods are very appealing in nano-optics and plasmonics as they enable high-resolution, nanoscale mapping of modes in metallic nanostructures [16], [51], [52], [60]–[65]. Accurate interpretation of CL arising from geometrically-induced plasmonic effects requires understanding the bulk optical response.

We begin our analysis by presenting CL spectra of bulk metal samples, including the transition metals Au, Ag, Cu, platinum (Pt), nickel (Ni), and chromium (Cr), as well as the post-transition metals such as aluminum (Al) and titanium (Ti). Figure 6a-h show the CL spectra of these metals across a range of electron beam energies from 1 keV to 30 keV. A common trend observed in the CL spectra of these metals is that the intensity generally decreases at longer wavelengths [66], a behavior governed by the dielectric response of the interface material. In metals like Au and Cu, interband transitions from occupied *d*-bands to the partially filled *sp*-band increase absorption at shorter wavelengths, thus reducing the transition radiation intensity [39]. At the high electron beam energy of 30 keV, CL spectra are broadband in all the tested metals, which is characteristic for the transition radiation with the distinctive dipolar, doughnut-shaped, angular radiation profile integrated over entire spectral range (green in Figure 6i-p). This occurs because faster electrons interact more strongly with the dense metal structure, generating stronger transition radiation as they cross the vacuum-metal interface [6], [67].

At the lower electron beam energies, the contribution of transition radiation to the CL spectra is significantly reduced [68]. At 1 keV, we observe a perfectly isotropic angular radiation profile for Ag (blue in Figure 6j) and mixed isotropic-dipolar angular profiles for Au and Cu (Figure 6i

and k), which are transition metals from group 11 of the periodic table. This indicates a surface-related and incoherent origin of CL at 1 keV. The CL spectra of Au and Cu exhibit well-resolved peaks around 500 nm and 590 nm, respectively, superimposed on the broadband transition radiation spectrum. These results align well with previous CL measurements on thin metal films [69], suggesting that this radiation stems from interband recombination in Au and surface-related emission of natural oxide layers in Ag and Cu [43]. The post-transition metals Al and Ti also display isotropic emission profiles at 1 keV, likely originating from their natural oxide surface layers. Finally, the transition metals from the group 10 of periodic table Pt, Ni, and Cr, exhibit the broad transition radiation spectra at 1 keV (Figure 6f-h) with the characteristic doughnut-shaped angular radiation profile (blue in Figure 6n-p). This is likely because they have closed orbitals, making them chemically inert under normal conditions and preventing the formation of oxides or other surface compounds.

5.2 Elemental metalloids

Elemental metalloids silicon (Si) and germanium (Ge) are group 14 elements in the periodic table, sharing the same valence electron configuration and exhibiting semiconductor behavior with an indirect bandgap. Previous CL studies of Si and Ge focused on their optical and electronic properties, especially concerning defect states, impurity levels, strain distributions, offering a high spatial resolution method to assess carrier lifetimes and electronic transitions [1], [70]. These experiments used significantly higher beam currents ranging from 100 nA to 10 μ A, with electron energy adjustments allowing for depth profiling.

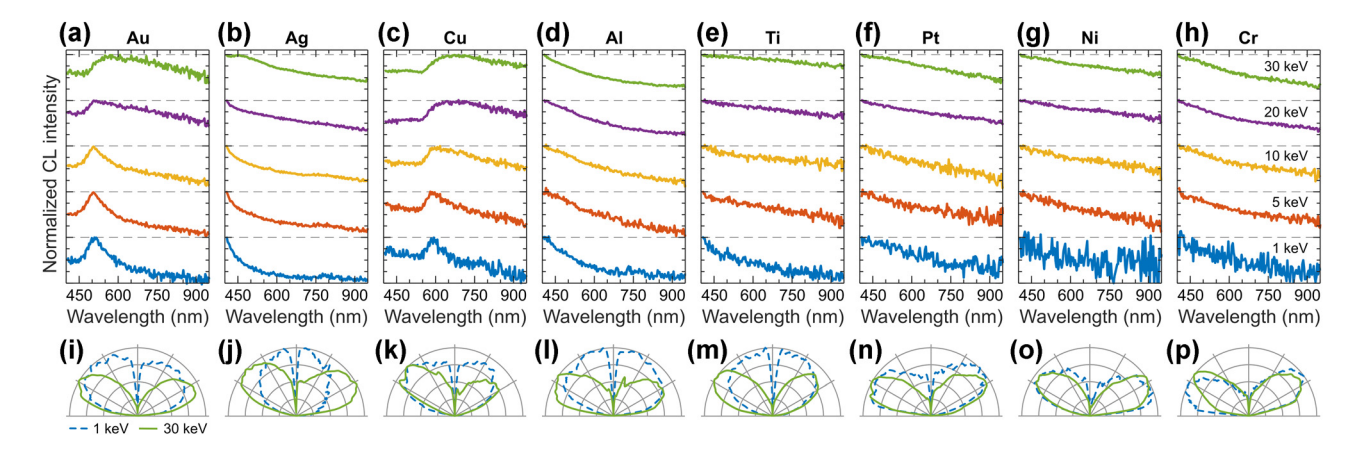


Figure 6: CL of elemental metals. Normalized CL spectra measured in a range of electron beam energies (see panel (h) for color coding, the spectra are vertically offset for clarity of presentation) for: (a) mono-crystalline Au, (b) Ag, (c) Cu, (d) Al, (e) Ti, (f) Pt, (g) Ni, (h) Cr. (i–p) Corresponding angular radiation profiles measured at 1 keV (dashed blue) and 30 keV (solid green).

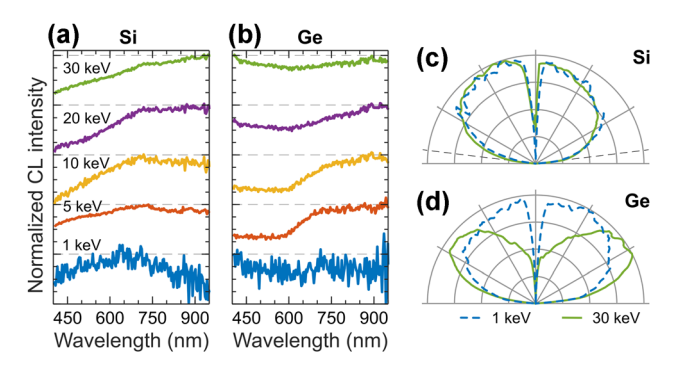


Figure 7: CL of elemental metalloids. Normalized CL spectra measured in a range of electron beam energies for: (a) Si, and (b) Ge. (c–d) Corresponding angular radiation profiles measured at 1 keV (dashed blue) and 30 keV (solid green).

We report CL from bulk Si and Ge crystals in Figure 7a and b, generated at low beam current of ca. 1.4 nA, in contrast to the previous studies. Figure 7c and d show angular radiation profiles of Si and Ge, which are a linear mix of isotropic and dipolar emission patterns [18], [19]. The isotropic contribution from incoherent CL originates from indirect bandgap transitions in these materials with bandgap energies corresponding to the IR part of electromagnetic spectrum. The dipole emission from coherent CL stems from the transition radiation, which dominates at shorter wavelengths. We confirm this in spectral filtering experiments by separating the incoherent and coherent CL with optical filters (SM Figure S11). In summary, the CL emission of bulk Si and Ge consists of a combination of incoherent isotropic radiation from indirect bandgap transitions and coherent dipole-like emission from transition radiation, which can be separated using spectral filtering.

5.3 Topological insulators

Topological insulators are materials that behave as insulators in their bulk form but have conductive states on their surfaces, protected by topological order, making them suitable for applications in quantum computing and photonics [71]. CL investigation of topological insulators allows for probing of their electronic band structure properties, defect states, exciton polaritons, and surface phenomena, providing insights into the unique optical and quantum properties of topological states [72]–[75].

We report CL response of bismuth telluride (Bi_2Te_3) and antimony trisulfide (Sb_2S_3) crystals in Figure 8a and b. Bi_2Te_3 in Figure 8a exhibits broadband CL similar to elemental metals indicating on transition radiation origin of CL signal, which is further confirmed by the characteristic doughnut-shaped angular radiation profile in Figure 8c.

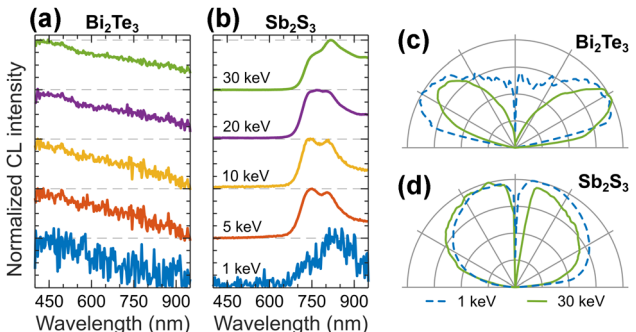


Figure 8: CL of topological insulators. Normalized CL spectra measured in a range of electron beam energies for: (a) Bi₂Te₃, and (b) Sb₂S₃. (c–d) Corresponding angular radiation profiles measured at 1 keV (dashed blue) and 30 keV (solid green).

In contrast, Sb_2S_3 crystal exhibits bright CL with spectrum peaking in the near IR spectral region (Figure 8b), corresponding to the quasi-direct bandgap emission [76]. The CL of Sb_2S_3 is characterized by isotropic angular radiation pattern (Figure 8d), confirming the incoherent, bandgap-related origin.

5.4 TMD crystals

Transition metal dichalcogenide (TMD) materials are 2D layered crystals, where the layers are weakly bonded by van der Waals forces, allowing them to be exfoliated down to a monolayer. Electron beam excitation is inherently inefficient in TMD monolayers due to their extreme thinness, which results in an exceptionally short electron interaction length. Encapsulation with hexagonal boron nitride (hBN) increases the interaction length, enabling electronhole pairs to form in the hBN, which then decay through the TMD monolayer generating CL [77]. Such CL studies have focused on exciton dynamics in monolayers, strain effects, and electron-hole interactions at the nanoscale, providing insights into their optical properties [26], [77]-[82]. CL methods have been also applied in nano-optics research involving multilayer TMD flakes, which support various optical modes depending on their shape and thickness [58], [83]–[86]. However, the CL response of bulk TMD crystals remains relatively underexplored, yet it is essential for establishing a reliable reference for CL experiments in photonics and plasmonics.

We report the CL emission properties of bulk TMDs in Figure 9, including semiconductor TMDs such as tungsten disulfide (WS₂), molybdenum disulfide (MoS₂) [both the rhombohedral (3R) and the hexagonal (2H) symmetry phases], tungsten diselenide (WSe₂), molybdenum diselenide (MoSe₂), rhenium disulfide (ReS₂), as well as semimetal and metal TMDs such as molybdenum

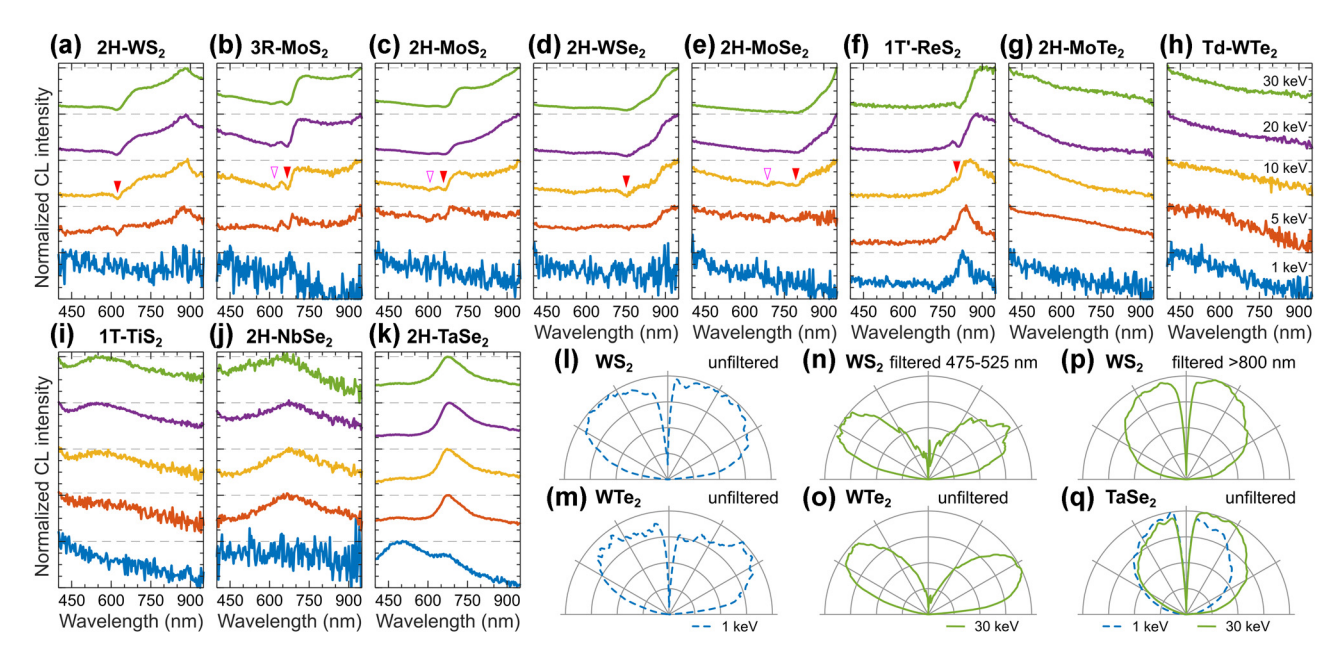


Figure 9: CL of TMD crystals. Normalized CL spectra measured in a range of electron beam energies for a variety of TMD crystals: (a) 2H-WS, (b) 3R-MoS₂, (c) 2H-MoS₂, (d) 2H-WSe₂, (e) 2H-MoSe₂, (f) 1T'-ReS₂, (g) 2H-MoTe₂, (h) Td-WTe₂, (i) 1T-TiS₂, (j) 2H-NbSe₂, and (k) 2H-TaSe₂. Spectral dips corresponding to excitons X_A (red triangle) and X_B (open magenta triangle) are indicated for relevant TMD crystals. (I–m) Mixed angular radiation profiles of WS₂ and WTe₂ at 1 keV. (n, p) Spectrally decomposed angular radiation profiles of WS₂ at 30 keV into (n) coherent and (p) incoherent CL, which are representative for the semiconducting TMDs. (o) Dipolar angular radiation profile of WTe2, which is representative for the semimetallic TMDs. (q) Isotropic angular radiation profile of TaSe₂ at 1 keV (dashed blue) and 30 keV (solid green).

ditelluride (MoTe₂), tungsten ditelluride (WTe₂), titanium disulfide (TiS₂), niobium diselenide (NbSe₂), and tantalum diselenide (TaSe2). For each investigated TMD crystal we identified its symmetry phase based on Raman spectra (see SM).

CL response of semiconducting TMD crystals (WS2, MoS₂, WSe₂, MoSe₂, ReS₂) exhibits a complex structure (Figure 9a-f), combining coherent and incoherent contributions as revealed from angular spectra measurements. Angular radiation profiles both at 1 keV and 30 keV measured in the broadband spectral range exhibit mixed isotropic-dipole patterns as in Figure 91 for WS2, while the spectral filtering experiments help to decompose them in coherent and incoherent contributions as in Figure 9n and p. CL intensity dominates at wavelengths longer than the expected A exciton line X_A in Figure 9a-f (marked by the red filled triangle), and we attribute this emission to electron-hole recombination near the bandgap energy. Therefore, this bandgap-related emission is characterized by incoherent CL with isotropic angular radiation profile, which we demonstrate on the example of a WS₂ crystal using a long-pass filter at 800 nm in Figure 9p. In contrast, at the wavelength below X_A, CL emission exhibits perfectly dipolar angular radiation profile, as shown for WS2 crystal measured with a band-pass filter at 475-525 nm in Figure 9n.

We repeated these optical filtering experiments for all the semiconducting TMD crystals from Figure 9a-f, confirming these CL emission properties (SM Figure S12).

Interestingly, we observe spectral dips at the position of A and B excitons in the semiconducting TMD crystals (indicated by the filled red and open magenta triangles in Figure 9a-f, respectively). We attribute these spectral features to self-absorption of bandgap-related emission in bulk TMD flakes by A and B excitons, which are consistent with refractometry measurements [87] (SM Figure S19). This is further supported by CL experiments of few layer MoS₂ on emissive substrates, where spectral dips were observed around the exciton energies [88]. Additionally, similar spectral dips have been reported in CL studies of thin TMD crystal slabs, attributed to strong exciton-photon coupling between cavity modes and excitons [83], [84].

Semimetallic and metallic TMD crystals (MoTe₂, WTe₂, TiS₂, NbSe₂) exhibit broadband CL emission (Figure 9g-j), similar to the CL response of metals. This CL emission has the coherent origin as confirmed by the dipolar angular radiation profiles as shown on the example of WTe2 in Figure 90 (see also SM Figure S12). In contrast, the TaSe₂ crystal is a metallic TMD that exhibits strong photoluminescence due to interband transitions [89]. We observe a similar response of TaSe₂ in CL with strong emission around 675 nm and isotropic angular radiation profile (Figure 9k and σ).

5.5 Boron nitride

Boron nitride (BN) exists in various structural forms, with cubic (cBN) and hexagonal (hBN) being the most commonly used in photonics due to their distinct optical and electronic properties. cBN has a structure similar to diamond, while hBN is a van der Waals layered material analogous to graphite. Both cBN and hBN have a wide bandgap (5.9-6.4 eV), which can host a variety of narrowline emitters operating at room temperature, making the BN platform highly suitable for quantum emitter engineering [90]–[99]. The high spatial resolution of CL methods aids in understanding defect-related emission while also providing insights into exciton behavior and phonon interactions at the nanoscale [100]-[104]. Additionally, the electron beam can create or activate defects in hBN [97]-[99], [104], unlocking potential for deterministic quantum emitter generation and integration with photonic and quantum devices. Furthermore, encapsulating TMD monolayers with hBN has enabled their efficient electron beam excitation [77].

We report the CL response of cBN and various hBN crystals sourced from different suppliers, along with observed narrow-line emission defects (Figure 10). Figure 10a-d present CL spectra of cBN and hBN crystals, which exhibit strong CL emission in the UV spectral region, in good agreement with previous CL studies [100]-[102]. We observe an isotropic angular radiation profile for this CL signal, as demonstrated on the example of an hBN crystal from HO Graphene in Figure 10f (see also SM Figure S13).

We examined multiple cBN and hBN crystals to identify defect sites characterized by narrow-line emission, as summarized in Figure 10e. In cBN micro-crystals (light blue in Figure 10e), we observe defect-related emission in the near-IR spectral range around 759 nm (1.634 eV), which may be associated with defects reported in Refs. [90], [93], along with a more prominent defect emission centered around 770 nm (1.610 eV), which, to the best of our knowledge, has not been previously reported. In hBN crystals from 2D Semiconductors (red in Figure 10e), we observe blue defects with a CL spectrum centered around 419 nm and 440 nm, which are related to nitrogen interstitial defects or B centers and can be electron-beam induced [98], [105]. We observe similar defects in hBN crystals from HQ Graphene (green in Figure 10e) and in hBN micropowder from 2D Semiconductors (black in Figure 10e). Finally, we observe a bright defect emission centered around 533 nm in hBN crystals from all suppliers, exhibiting an isotropic angular radiation profile (Figure 10g). Activation of this defect by an electron beam has been reported in Ref. [99], whereas we were able to induce its formation using an electron beam at ca. 1.4 nA in mechanically exfoliated hBN crystals regardless of the sample source (HQ Graphene or 2D Semiconductors).

5.6 Diamond and graphite

Carbon forms a variety of allotropes, such as diamond and graphite, each exhibiting unique and rich optoelectronic properties [106], [107]. Diamond, an insulator with a wide bandgap (5.5 eV), is among the most extensively studied materials in CL microscopy [13], [108]. It serves as a prominent platform for quantum emitter engineering, as its wide bandgap can host stable narrow-line emitters at room temperature, making it valuable for quantum technology applications [109]. Additionally, CL from these defects enables the study of the fundamental physical properties of electron-induced incoherent light emission [25], [36], [110], [111]. Graphite, the hexagonal allotrope of carbon, exhibits

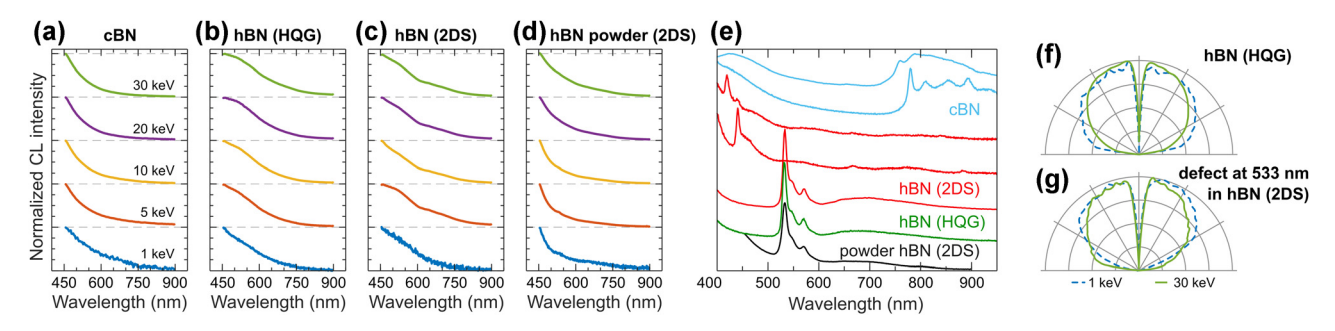


Figure 10: CL of cBN and hBN crystals. Normalized CL spectra measured in a range of electron beam energies for: (a) micro-crystals of cBN; (b) hBN crystal from HQ Graphene (HQG); (c) hBN crystal from 2D Semiconductors (2DS); (d) hBN power from 2DS. (e) Normalized CL spectra of various defects and color centers measured from cBN (blue), hBN from 2DS (red), hBN from HQG (green), and hBN powder from 2DS (black). (f-g) Isotropic angular radiation profiles measured at 1 keV (dashed blue line) and 30 keV (solid green line) for hBN crystal from HQG and electron-beam-induced defect emission in hBN crystal from 2DS.

semimetallic characteristics and has primarily been studied for its CL properties in geological investigations [112], [113].

We report the CL response of synthetic diamond crystals from ThermoFisher and Adamas Nanotechnologies (Figure 11). The ThermoFisher diamonds are relatively large, measuring tens of microns across, and are not intentionally doped, allowing us to study the bulk CL response of diamond. Their CL spectra, shown in Figure 11a, peak in the UV region beyond our detection range. The bulk CL response is often accompanied by broad defect emission around 430 nm and 515 nm (black and green in Figure 11b), which correspond to the A and green bands, respectively [106]. Occasionally, these crystals also exhibit narrow-line defect or impurity emission, among which we observe emission from H3, N3, and Ni-related centers (marked by red triangles in Figure 11b).

The diamonds from Adamas Nanotechnologies are submicron in size and are intentionally doped with NV and SiV centers at varying densities, enabling the isolation of single-photon emitters. Figure 11c presents the CL spectra of NV⁰ (574 nm), NV⁻ (638 nm), SiV⁻ (738 nm), and Si-related (722 nm) centers [36], [106], [114], [115], with some diamonds containing a mixture of these centers. Figure 11e shows a representative isotropic angular radiation profile of the NV⁰ center (see also SM Figure S14).

In contrast to diamond, the CL of graphite is much dimmer and is the weakest among all investigated materials in our atlas. Figure 11d shows the broadband CL spectrum of a graphite crystal, resembling the transition radiation observed in metals. The corresponding angular radiation profiles in Figure 11f are similar to those observed in metals and metalloids. The angular radiation profile at 30 keV is dipolar (green in Figure 11f), and, together with the broadband spectrum, suggests a coherent CL origin attributed to transition radiation.

5.7 Common glasses

CL methods are widely used for glass characterization, providing insights into their microstructural and optical properties [13], [116]. We report the CL response of SiO₂-based glasses in Figure 12. CL emission from SiO₂ is complex and originates from the luminescence associated with various defects [116] – [120]. Figure 12a presents CL spectra of a thin, 100 nm dry-grown oxide layer on Si, which is commonly used to exfoliate 2D materials, such as graphene and TMD monolayers. The three luminescent peaks in Figure 12a correspond to emission from non-bridging oxygen hole centers around 460 nm [117], [121], self-trapped excitons around 560 nm [121], and oxygen vacancies around 650 nm [117], [121]. Figure 12b shows CL spectra of α -quartz with a dominant peak around 650 nm, attributed to oxygen vacancies [116], [120].

Amorphous SiO2 is frequently modified through the incorporation of additional oxides to tailor its optical properties. We present CL spectra of SiO2-based borosilicate glasses, specifically the commercial brands Menzel-Gläser and BK7, as shown in Figure 12c and d. Assigning these CL spectra to specific defect emissions is challenging due to the complex structural composition of borosilicates, but the observed spectral peaks are generally associated with SiO₂-related defects [122]. Finally, Figure 12e shows isotropic angular radiation profiles of BK7, which are representative of all the glasses presented (see also SM Figure S15).

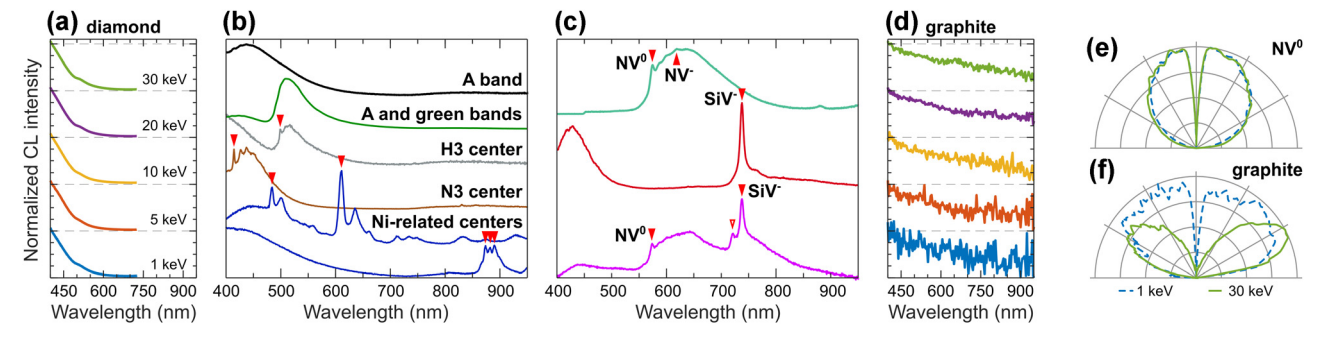


Figure 11: CL of diamond and graphite. (a) Normalized CL spectra of a diamond crystal (ThermoFisher), measured at various electron beam energies. Data above 725 nm was excluded due to strong second-order diffraction artifacts. (b) Defect emission in diamond crystals (30 – 60 µm across, Thermo-Fisher). (c) Color centers in doped nanodiamonds (<1 μm across, Adamas Technologies). The spectral positions of the emission lines discussed in the main text are marked with red triangles. (d) Normalized CL spectra of graphite crystal, measured at various electron beam energies (see panel (a) for color coding). (e) Isotropic angular radiation profile of NV⁰ color center in a diamond nanocrystal at 1 keV (dashed blue) and 30 keV (solid green), respectively, measured with a short pass filter at 600 nm. (f) Mixed angular radiation pattern at 1 keV (dashed blue) and dipolar at 30 keV (solid green) of graphite.

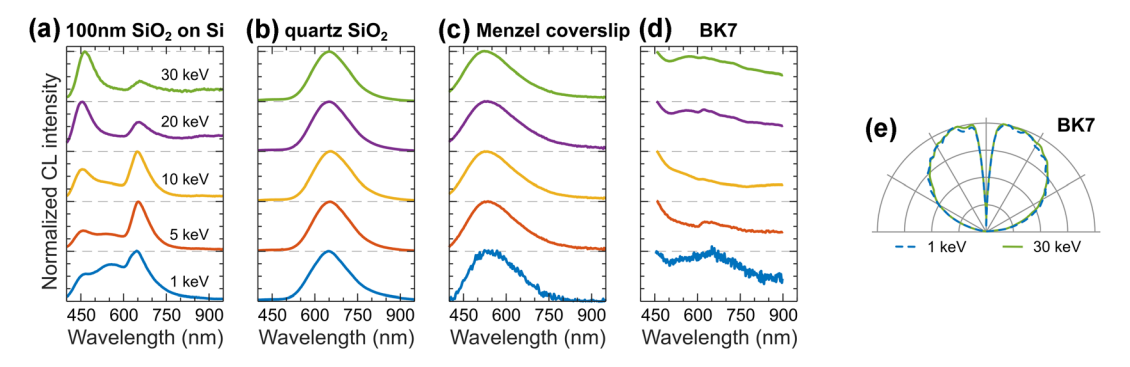


Figure 12: CL of common glasses. Normalized CL spectra measured in a range of electron beam energies for: (a) 100 nm-thick layer of SiO₂ on bulk Si, (b) α-quartz (SiO₂), (c) Menzel coverslip, and (d) BK7 glass. (e) Isotropic angular radiation profiles of BK7 glass at 1 keV (dashed blue) and 30 keV (solid green), representative for all materials in panels (a-d).

5.8 Silicon-based materials

We report the CL response of silicon-based materials, such as mica, silicon carbide (SiC), and silicon nitride (Si₂N₄), in Figure 13. Mica, a naturally occurring layered silicate, is used as an atomically flat substrate with a wide range of applications in photonics [123], and has also been employed to study Cherenkov and transition radiation generated in a transmission electron microscope [66]. Here we report CL of Muscovite mica (KO₂Al₂O₃SiO₂) in Figure 13a, which has broad spectra spanning the visible to near-IR regions with an isotropic angular radiation profile (SM Figure S16). This is indicative of an incoherent defect-related emission from oxide components in mica; notably, at higher electron beam energies, we observe an additional narrow-line emission around 764 nm.

SiC, a wide-bandgap semiconductor, finds applications in optoelectronics due to its high thermal conductivity and stability. SiC can also host a range of CL-active defect centers [124]-[126], such as the silicon vacancy and divacancy complexes, with potential for quantum information and sensing technologies [127]. While SiC exists in various structural polytypes, here we focus on the 4H and 6H phases, which are widely used in photonics. Figure 13b and c show the CL spectra of the 4H and 6H phases, respectively. These SiC phases exhibit similar spectral features, including two broad emission bands centered around 470 nm and 680 nm. The emission band around 470 nm originates from boron impurities in SiC, while the band near 680 nm is associated with basal plane dislocations [125], [126]. Additionally, an emission line appears around 918 nm in the 6H-SiC sample, likely originating from silicon vacancies [124].

Figure 13d-f presents the CL spectra of Si₃N₄ in various forms: α -Si₃N₄ micro-powder, compressed crystals of β - Si_3N_4 , and a 20 nm-thin Si_3N_4 membrane. α - and β - Si_3N_4 are used in low-loss photonics and support nano-structuring, having a wide bandgap (4.8-5.2 eV) and exhibiting defectrelated emission in CL [128]-[131]. Figure 13d presents CL spectra of α -Si₃N₄, with a strong emission band around 730 nm, and a minor peak around 540 nm, which are likely related to defect emission. Our α -Si₂N₄ sample also exhibits

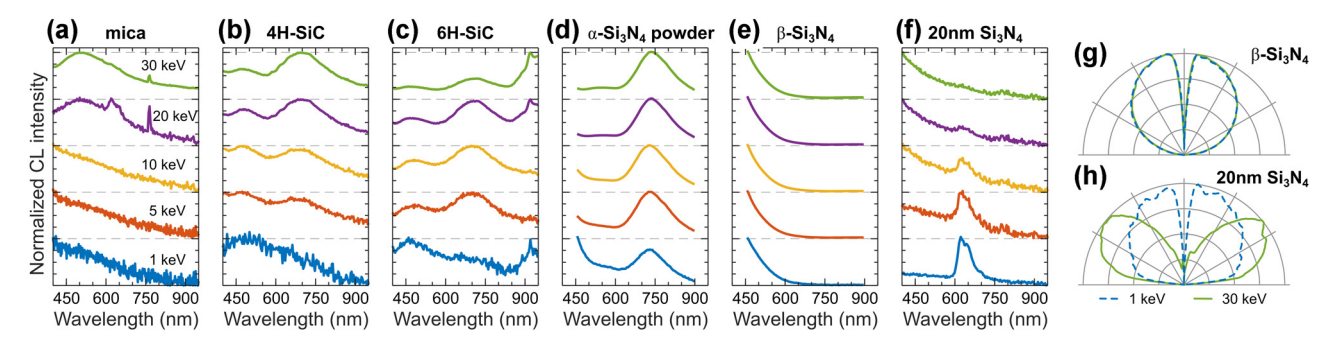


Figure 13: CL of silicon-based materials. Normalized CL spectra measured in a range of electron beam energies for: (a) mica, (b) 4H-SiC, (c) 6H-SiC, (d) α -Si₃N₄ nanopowder, (e) crystalline β -Si₃N₄, and (f) 20 nm-thin Si₃N₄ membrane. (g) Isotropic angular radiation profiles of β -Si₃N₄ at 1 keV (dashed blue) and 30 keV (solid green), representative for materials in panels (a-e). (h) Isotropic and dipolar angular radiation profiles of 20 nm-thin Si₃N₄ membrane at 1 keV (dashed blue) and 30 keV (solid green), respectively.

intense photoluminescence, preventing phase characterization via Raman microscopy (see corresponding spectrum in SM). In contrast, β -Si₃N₄ exhibits CL only in the UV region (Figure 13e), and shows no photoluminescence in the visible region. As a membrane, Si₃N₄ is commonly used in electron beam spectroscopy as a free-standing platform. With thicknesses down to 5 nm, it enables substrate-free CL measurements, minimizing background signals and improving sensitivity for optical mode characterization [21]. Therefore, its characterization is of particular importance for CL microscopy. Here we report CL of a 20 nm-thin Si₃N₄ membrane in Figure 13f. At low electron beam energies, it exhibits a CL peak around 620 nm, attributed to defectrelated emission; this peak disappears at higher energies, as electrons pass through the membrane without interaction. In contrast, the high energy electrons cause transition radiation at the vacuum-membrane interface [66], which we confirm with angular emission measurements. Figure 13h shows an isotropic angular emission profile for defect emission around 620 nm efficiently excited at 1 keV, whereas at 30 keV, a dipolar angular emission profile characteristic of transition radiation is observed.

5.9 Common photonic materials and optical coatings

Understanding bulk CL emission is crucial for differentiating it from geometry-tailored emission arising from optical modes and resonances or from broadband transition

radiation. We report CL response for common photonic materials and optical coatings in Figure 14, covering a broad range of semiconductors and dielectrics employed in photonic and plasmonic devices. We further divide this section into subsections, each focused on a specific material category, including oxides, gallium derivatives, fluorides, and nitrides.

5.9.1 Oxides

We selected widely used oxides in photonics and nanotechnology such as indium tin oxide (ITO), titanium dioxide (TiO2), zirconium dioxide (ZrO2), tantalum pentoxide (Ta₂O₅), molybdenum trioxide (MoO₃), lithium niobate (LiNbO₃), aluminum oxide (Al₂O₃), and ytterbium oxide (Yb₂O₃), presenting their respective CL spectra along with their interpretation.

Figure 14a shows CL spectra of ITO, which combines optical transparency and electrical conductivity, functions as an epsilon-near-zero (ENZ) material, and offers tunable plasmonic properties in the near IR. The broad CL spectra from ITO are characterized by an emission band centered around 500 nm, attributed to its indirect bandgap and varies between 2 and 3.5 eV, depending on the exact doping composition of ITO [132], [133].

Figure 14b shows CL spectra of anatase-TiO2, which exhibits a high refractive index, wide bandgap, strong photocatalytic activity, and the ability to support localized surface plasmon resonances when doped. The CL from

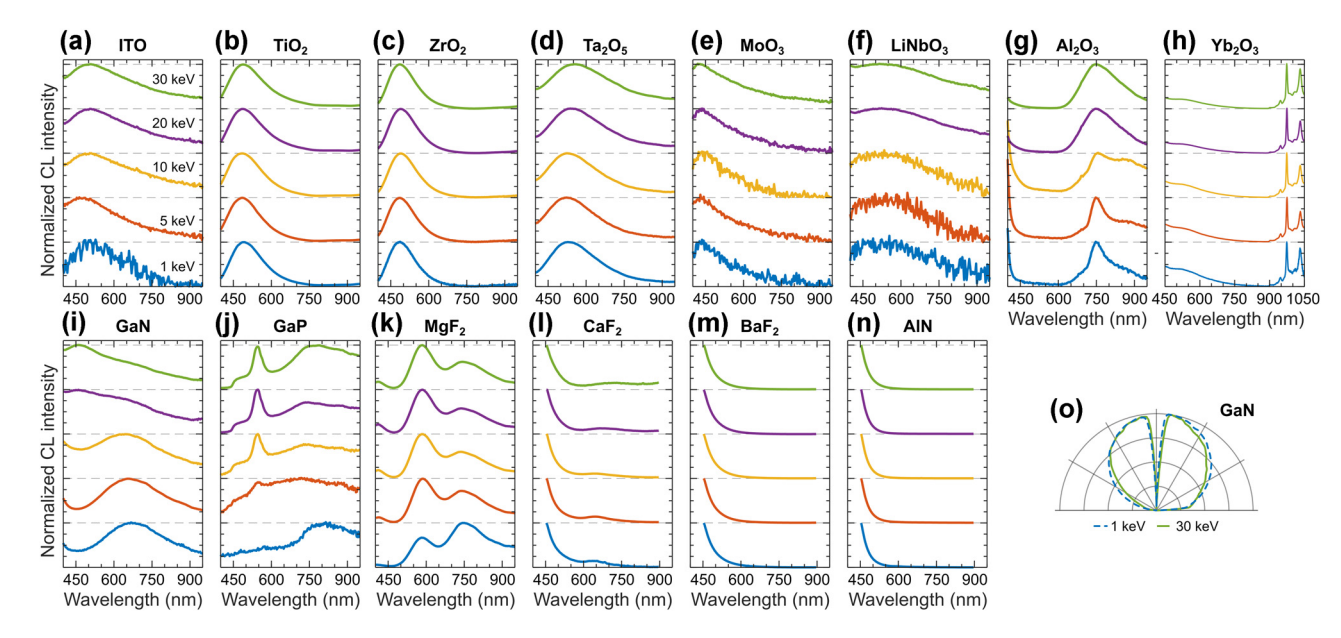


Figure 14: CL of common photonic materials and optical coatings. Normalized CL spectra measured in a range of electron beam energies for: (a) ITO, (b) TiO₂, (c) ZrO₂, (d) Ta₂O₅, (e) MoO₃, (f) LiNbO₃, (g) α -Al₂O₃, (h) Yb₂O₃, (i) GaP, (k) MgF₂, (l) CaF₂, (m) BaF₂, and (n) AlN. (o) Isotropic angular radiation profiles of GaN at 1 keV (dashed blue line) and 30 keV (solid green line), representative for all materials in panels (a – n).

anatase exhibits an emission band centered around 490 nm, likely related to emission from Ti^{3+} ions, while the tail in the visible region is associated with oxygen vacancy centers and oxygen interstitials [134]–[136].

Figure 14c shows CL spectra of ZrO_2 , a high-temperature, chemically stable ceramic with a high dielectric constant and optical transparency. The CL from ZrO_2 exhibits an emission band centered around 485 nm, originating from intrinsic oxygen vacancies within the bandgap [137], [138].

Figure 14d shows CL spectra of Ta_2O_5 , a high-refractive-index dielectric with excellent insulating properties and transparency from the visible to IR range. The CL from Ta_2O_5 exhibits a broad emission band centered around 560 nm at 30 keV, slightly blueshifting to 540 nm at 1 keV, likely originating from defects within the oxide structure, such as oxygen vacancies or tantalum luminescence centers [139]. As with other oxides, oxygen vacancy formation within the 3.75 eV bandgap can strongly influence its optical response [140], contributing to the observed CL.

Figure 14e shows CL spectra of MoO_3 , which is characterized by a high refractive index, tunable bandgap, strong birefringence, and the ability to support surface plasmon polaritons. The CL from MoO_3 exhibits a broad emission band spanning from the UV to the visible region, originating from its 3 eV bandgap [141], [142].

Figure 14f shows CL spectra of LiNbO₃, which is characterized by a high refractive index, strong nonlinear optical coefficients, and excellent electro-optic properties. The CL from LiNbO₃ exhibits a broad emission band peaking around 540 nm and a shoulder extending into the near-IR, primarily originating from defect-related emission [143].

Figure 14g shows CL spectra of α -Al $_2$ O $_3$, the crystalline polymorph of sapphire. It is characterized by high transparency across a wide spectral range, exceptional hardness, high thermal stability, and excellent dielectric properties. The CL from α -Al $_2$ O $_3$ features a band in the UV region related to oxygen vacancies center and a band centered around 750 nm attributed to Ti $^{3+}$ impurities [144], [145]. The band at 750 nm is broad at 30 keV and becomes narrower as the electron energy decreases. We also observe a narrow emission line around 690 nm, attributed to Cr $^{3+}$ impurities [144], [145].

Figure 14h shows CL spectra of Yb_2O_3 , which is characterized by a high refractive index, a wide bandgap, efficient luminescence, and a high rare-earth doping potential [146]. The CL from Yb_2O_3 exhibits a broad spectral band centered in the UV spectral region. Additionally, we observe bright narrow spectral lines at 947 nm, 976 nm, 1,009 nm,

and 1,033 nm in the near-IR region; due to their high brightness, the detection range for Yb_2O_3 was extended up to 1,050 nm in Figure 14h. These lines align well with the emission spectrum of the 4f-electron levels of Yb^{3+} , where the brightest emission at 976 nm corresponds to the ${}^2F_{7/2} \rightarrow {}^2F_{5/2}$ transition [147].

5.9.2 Gallium derivatives

Gallium (Ga) is primarily used in the form of III–V compound semiconductors, such as the gallium nitride (GaN) and gallium phosphide (GaP). Figure 14i shows CL spectra of GaN, which is characterized by a wide direct bandgap, high thermal conductivity, strong emission in the UV-visible range, and the ability to support surface plasmon polaritons. The CL exhibits a broad emission band centered around 630 nm at 1 keV relating to the ubiquitous defect and impurity emission in GaN [148]–[150].

Figure 14j shows CL spectra of GaP, which is characterized by an indirect bandgap with a high refractive index, high optical transparency, and strong dielectric properties, making it attractive material for optical nanoantennas. The CL from GaP exhibits a narrow peak at 548 nm superimposed on a broad band centered around 750–800 nm. The emission peak at 548 nm is characteristic of free exciton recombination from the indirect bandgap of GaP at room temperature [151]. The broadband emission can originate from various impurities and defects [152], [153]. Depending on the electron beam energy in Figure 14j, a different composition of impurities and defects alters the emission spectrum.

5.9.3 Fluorides

Fluoride materials have emerged as an important class of non-oxide glasses, offering a wide optical transmission bandwidth from the UV to IR, a low refractive index, and excellent durability, enabling numerous applications in photonics. We report CL of magnesium fluoride (MgF $_2$), calcium fluoride (CaF $_2$), and barium fluoride (BaF $_2$) in Figure 14k–m. The observed CL emission originates from structural defects and vacancy centers [154]–[156].

5.9.4 Nitrides

We have previously presented nitride materials such as BN, $\mathrm{Si}_3\mathrm{N}_4$, and GaN. Here, we conclude with aluminum nitride (AlN), which is widely used in photonics due to its large bandgap of approximately 6.6 eV and broad transmission

range [157]. The cathodoluminescence of AlN is characterized by a bright emission coming from the UV spectral region (see Figure 14n) and is usually attributed to the emission from oxygen color centers and aluminum vacancies [145], [148], [158].

Finally, Figure 140 shows the isotropic angular radiation profile of GaN, representative of all materials in this section, and indicating the incoherent origin of CL (see also SM Figure S17).

5.10 Polymeric and resist materials

Polymeric and resist materials are widely used in photonics, plasmonics, and nanotechnology fabrication as patternable substrates for lithography, enabling the creation of fine nanoscale features and complex optical structures. The materials selected here include polydimethylsiloxane (PDMS), poly(bisphenol A carbonate) or polycarbonate (PC), carbon tape (SPI Supplies), hydrogen silsesquioxane (HSQ), poly(methyl methacrylate) (PMMA), and the commercial photoresist SU8-2000 (Kayaku Advanced Materials). Awareness of their respective CL signals is of high importance, as these materials may serve as components in photonic and plasmonic devices or appear as residuals within them. Reliable CL measurements in polymeric materials require a tailored approach to prevent rapid degradation from extended electron beam exposure, which can significantly reduce signal intensity [159], [160]. An effective approach to mitigate this challenge is scanning a larger surface area of the polymer, capturing luminescence over a wider region to preserve signal quality while minimizing material damage.

The CL in polymers can arise from various mechanisms, one of which involves the formation of excitonic states that, upon relaxation to their ground state, generate light [159], [161]. The electron beam may also induce impact ionization of molecules, leading to luminescent recombination with secondary and backscattered electrons [161], [162], or the formation of a new luminescent molecule as a result of a chemical transformation [163]. These mechanisms exclude coherent CL processes in the emission from polymers that result in completely isotropic emission profiles in the angular resolved emission (see Figure 15g and SM Figure S18). CL measurements can induce structural changes in polymer resists, such as chain scission and crosslinking, potentially altering peak positions, intensities, or introducing new spectral features. To minimize beaminduced degradation, all measurements were performed using fuzzing (raster scanning within each pixel) combined with used beam currents (1.4 nA) and short acquisition times (1 s per 5 \times 5 μ m² area), corresponding to a calculated dose below 0.06 nC/ μ m² – well within the safe regime under electron irradiation [164]. To further mitigate cumulative effects, we shifted to adjacent sample regions between acquisitions.

Figure 15 presents CL response of selected polymeric and resist materials. Figure 15a shows the CL of PDMS, a silicon-based polymer with high optical transparency, elasticity, and heat resistance. PDMS is widely used for the exfoliation of TMD monolayers, graphene, and 2D material assembly [165], [166], as well as for the fabrication of layered organic optoelectronic devices [167]. PDMS exhibits bright and broad CL, with a peak around 595 nm and a shoulder centered around 460 nm. Figure 15b shows the CL from PC, a thermoplastic polymer containing carbonate groups, commonly used in the pick-up assembly of van der Waals heterostructures [165]. The CL of PC is characterized by a broad peak around 530 nm. Carbon tape is a conductive carbon-acrylic mixture used for mounting samples in electron beam-based techniques. Figure 15c shows the CL signal of carbon tape, which exhibits a broad emission band centered around 590 nm. Figure 15d shows the CL response of HSQ, a resist material with a cage-like structure and chemical composition of $[HSiO_{3/2}]_{2n}$ [168]. The CL spectra of HSQ in Figure 15d exhibit features as other SiO₂ derivatives in Figure 12. CL from HSQ has been observed

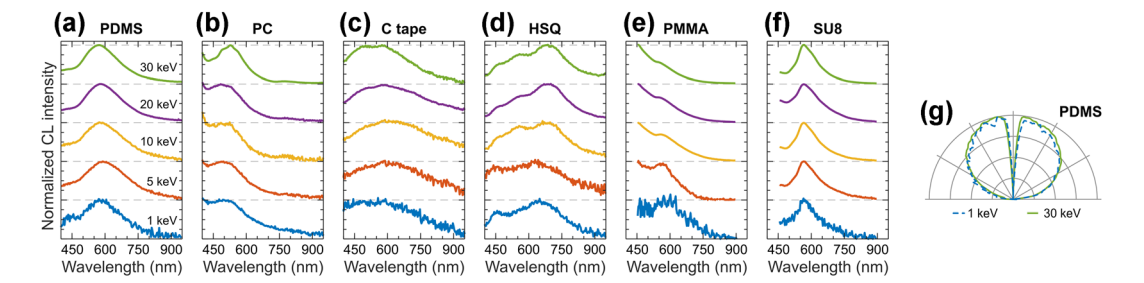


Figure 15: CL of polymeric and resist materials. Normalized CL spectra measured in a range of electron beam energies for: (a) PDMS, (b) PC, (c) carbon tape, (d) HSQ, (e) PMMA, and (f) SU8. (g) Isotropic angular radiation profiles of PDMS at 1 keV (dashed blue) and 30 keV (solid green), representative for all materials in panels (a-f).

in nanostructures used as a platform for generating sub-keV electron beam-induced Smith–Purcell radiation [169]. PMMA is a thermoplastic resist material that is used in photo and electron beam lithography [170]. The CL from PMMA is shown in Figure 15e, exhibiting bright emission in the UV spectral region and extending into the visible region. We also observe a local emission maximum around 560 nm, attributed to emissions from C=C bonds formed due to electron irradiation [163]. Figure 15f shows CL spectra of SU8-2000, a photo- and electron-beam resist material [171]. The CL from SU8 features a broad emission band centered around 565 nm.

6 Cathodoluminescence intensity

Now we turn our discussion to the response of CL intensity to electron beam current and energy. The dependence of CL intensity on electron beam current is typically linear [13], [172], [173], as higher currents increase the probability of electron interactions with the material, leading to brighter luminescence. However, this trend may deviate depending on the CL mechanism, exhibiting sub- as well as superlinear trends [149], [174], [175]. The relationship between CL intensity and electron beam energy can follow a more complex trend. At low beam energies, CL intensity is primarily influenced by shallow electron penetration and scattering effects. In contrast, at higher energies, a larger material volume contributes to radiative recombination, while deeper electron penetration reduces energy loss to backscattered and secondary electrons [173]. Moreover, at higher electron beam energies, photons are generated deeper within the material, increasing their travel distances and the likelihood of reabsorption. As a result, CL intensity may saturate or even decrease due to self-absorption effects, particularly in materials with high optical absorption coefficients [176]. Understanding CL intensity dependencies on current and energy is necessary for optimizing CL microscopy, as they influence the resolution, sensitivity, and interpretability of the CL signal.

We investigate the dependence of CL intensity on electron beam current and energy for Pt, an hBN-encapsulated WSe₂ monolayer, a bulk 3R-MoS₂ crystal, and GaP. The CL spectra of these materials at 10 keV are presented in Figure 16a–d, using comparable intensity scales. These materials were selected as they represent the primary sources of CL, including transition radiation, excitonic emission, bandgap-related emission, and defect-related emission. Figure 16a shows a typical broadband CL spectrum of transition radiation measured from bulk Pt, fitted with a function inversely proportional to the emitted wavelength

[66], i.e., $I_{\rm CL}(\lambda) \sim 1/\lambda$. This fitting function allows us to extract the CL intensity I_{CL} by integrating over the wavelength range from 400 nm to 950 nm. Figure 16e shows the evolution of the obtained CL intensity with electron beam current I at a fixed electron beam energy of 10 keV. We fit the data using a power law function of the form $I_{\rm CL}(I) \sim$ $(I/I_{\rm n})^{m_{\rm I}^{\rm TR}}$, where $I_{\rm n}$ denotes the reference current. Figure 16i presents the results of CL intensity measurements for Pt where the electron beam current is fixed at 1.4 nA while the electron beam energy E is varied. Likewise, we fit the obtained CL intensity dynamics using a power law function of the form $I_{\rm CL}(E) \sim (E/E_0)^{m_{\rm E}^{\rm TR}}$, where E_0 denotes the reference energy. The CL intensity fits for electron beam current and energy dependencies yield the scaling exponents m, summarized for all tested materials in Table 1. For transition radiation, we observe a linear dependence of CL intensity on both electron beam current and energy, with the scaling exponent *m* close to 1.

Figure 16b presents a narrow CL spectrum for exciton recombination in an hBN-encapsulated WSe2 monolayer on a Si substrate. THe hBN-WSe2 heterostructure is needed to generate CL because the monolayer is too thin to capture sufficient electron beam energy directly, so the electron beam excites carriers in the wide bandgap hBN, which then recombine through the monolayer to produce CL [77], [80]. To extract the CL intensity, we fit the spectrum with a two-Gaussian function, where the two components represent the neutral exciton and trion contributions to the CL spectrum [177]. Figure 16f and j present the results of CL intensity measurements at fixed electron beam energy and current, respectively. The power law fit in Figure 16f reveals a linear increase in exciton emission intensity with electron beam current. In contrast, Figure 16j shows a decrease in exciton emission intensity with increasing electron beam energy, also following a power law but with a negative exponent. The excitation of the hBN-WSe2 heterostructure is less efficient at higher electron energies because electrons pass through it without significant interaction and deposit their energy deeper in the Si substrate, where it does not contribute to monolayer excitation.

Figure 16c presents the complex CL spectrum of a bulk $3R\text{-}MoS_2$ crystal, similar to that reported in Figure 9b. Angular spectrum measurements, shown in Figure 9n and p (see SI Figure S12), confirm that the blue part of the emission spectrum has a coherent origin, while the red part originates from incoherent processes. Consequently, we attribute the blue part of the CL spectrum to transition radiation, the red part to the direct and indirect bandgap recombination – both of which can coexist in bulk $3R\text{-}MoS_2$ – and the spectral dips to absorption by A and B

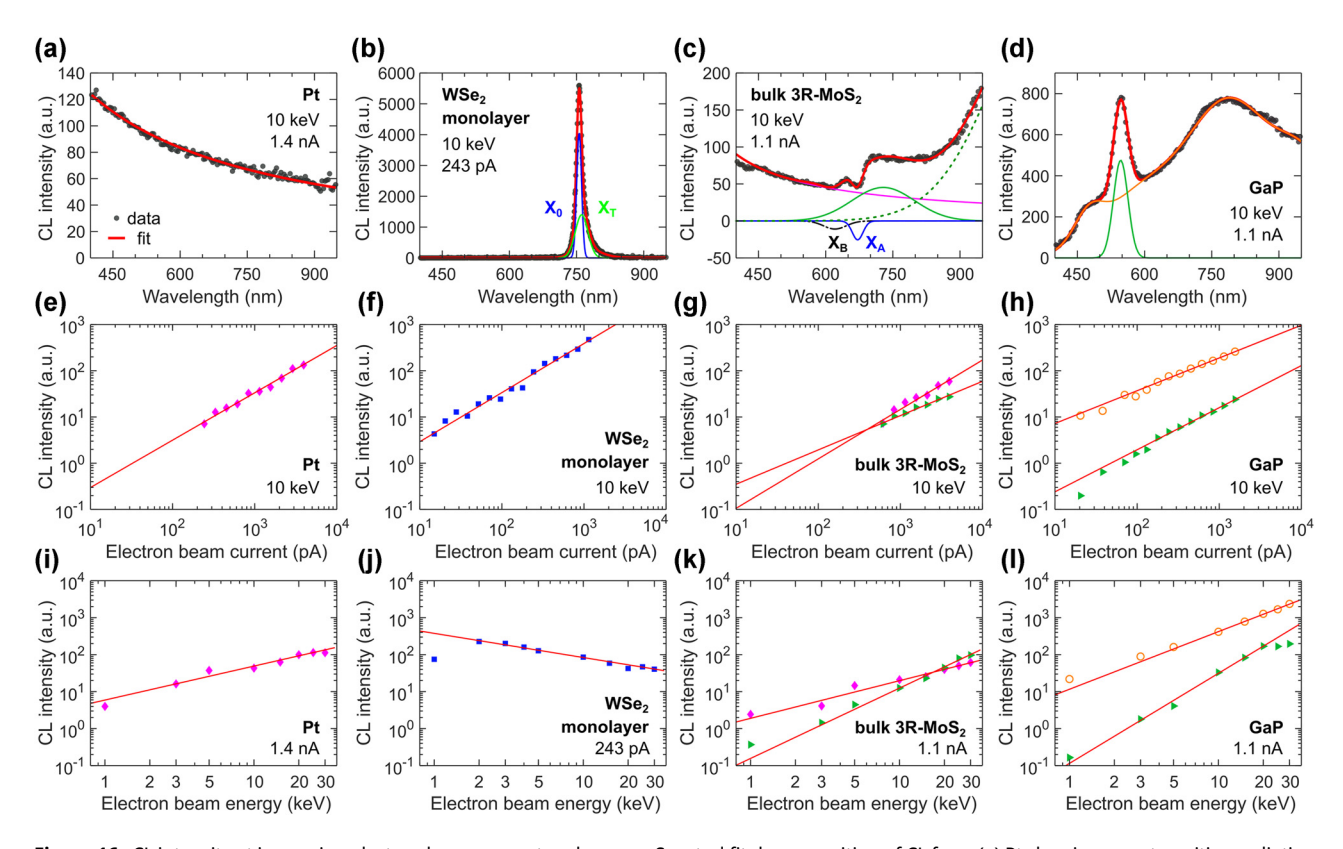


Figure 16: CL intensity at increasing electron beam current and energy. Spectral fit decomposition of CL from (a) Pt showing pure transition radiation, (b) hBN-encapsulated WSe₂ monolayer where peaks correspond to the neutral exciton X_0 (blue) and trion X_T (light green), (c) bulk 3R-MoS₂ with mix of transition radiation (magenta), direct (dashed green) and indirect (solid green) bandgap emission, and absorption peaks for X_A (solid blue) and X_B (dash-dotted black), and (d) GaP with indirect bandgap (green) and defect emission (black). The cumulative spectral fits are shown in red. Evolution of CL intensity with electron beam current (e-h) and voltage (i-l) for (e, i) transition radiation in Pt (magenta diamonds), (f, j) excitonic emission in WSe₂ monolayer (blue squares), (g, k) bulk 3R-MoS₂ with mixed transition radiation (magenta diamonds) and bandgap-related emission (green triangles), and (h, l) GaP with mixed indirect bandgap (green triangles) and defect emission (orange circles). The red lines represent power law fits; see text for details.

Table 1: Power law fitting of CL intensity evolution at increasing electron beam current $(m_{\rm I})$ and energy $(m_{\rm E})$. The superscript in scaling exponent m stands for emission of transition radiation (TR), excitons (X), bandgap-related emission (BG), and defects (D).

Material	$m{m}_{ m I}^{ m TR}$	$m{m}_{\mathrm{E}}^{\mathrm{TR}}$	$\textit{m}_{\mathrm{I}}^{\mathrm{X}}$	$\textit{\textbf{m}}_{\mathrm{E}}^{\mathrm{X}}$	$\emph{m}_{\mathrm{I}}^{\mathrm{BG}}$	$\textit{m}_{\mathrm{E}}^{\mathrm{BG}}$	$\textit{\textbf{m}}_{\mathrm{I}}^{\mathrm{D}}$	$m_{\rm E}^{ m D}$
Pt	1.02	0.92	-	-	-	-	-	_
WSe ₂ monolayer	-	-	1.06	-0.65	-	-	-	-
Bulk 3R-MoS ₂	0.96	1.06	-	-	0.70	1.90	-	-
GaP	-	-	-	-	0.91	2.44	0.71	1.56

excitons [87]. Therefore, we fit the complex CL spectrum in Figure 16c as a sum of contributions from (i) transition radiation, modeled as $\sim 1/\lambda$ (magenta), (ii) bandgap-related transitions, represented by two Gaussian peaks (solid and dashed green), and (iii) A and B exciton absorption peaks, modeled as negative Gaussians (solid blue and dashed black, respectively). This spectral decomposition enables us to distinguish between the coherent (transition radiation) and incoherent (bandgap-related emission) contributions to the

CL intensity, plotted in Figure 16g and k by magenta diamonds and green triangles, respectively. We apply a power law fit and obtain a linear dependence of transition radiation intensity on the electron beam current and energy in Figure 16g and k, which agrees well with the results for bulk Pt. The intensity of bandgap-related emission exhibits sublinear dependence on current and super-linear dependence on energy (Table 1).

Figure 16d presents the CL spectrum of GaP, where CL intensity originates from the indirect bandgap emission around 546 nm and broad defect emission. We fit the CL spectrum in Figure 16d as the sum of a Gaussian for the indirect bandgap emission (green) and four Gaussians for the broad defect emission (orange). Figure 16h and l present the results of spectral decomposition highlighting the contributions from indirect bandgap emission (green triangles) and defect emission (orange circles). The evolution of CL intensity for indirect bandgap and defect emission contributions with increasing electron beam current and energy are fitted with a power law, a sub-linear intensity dependence on

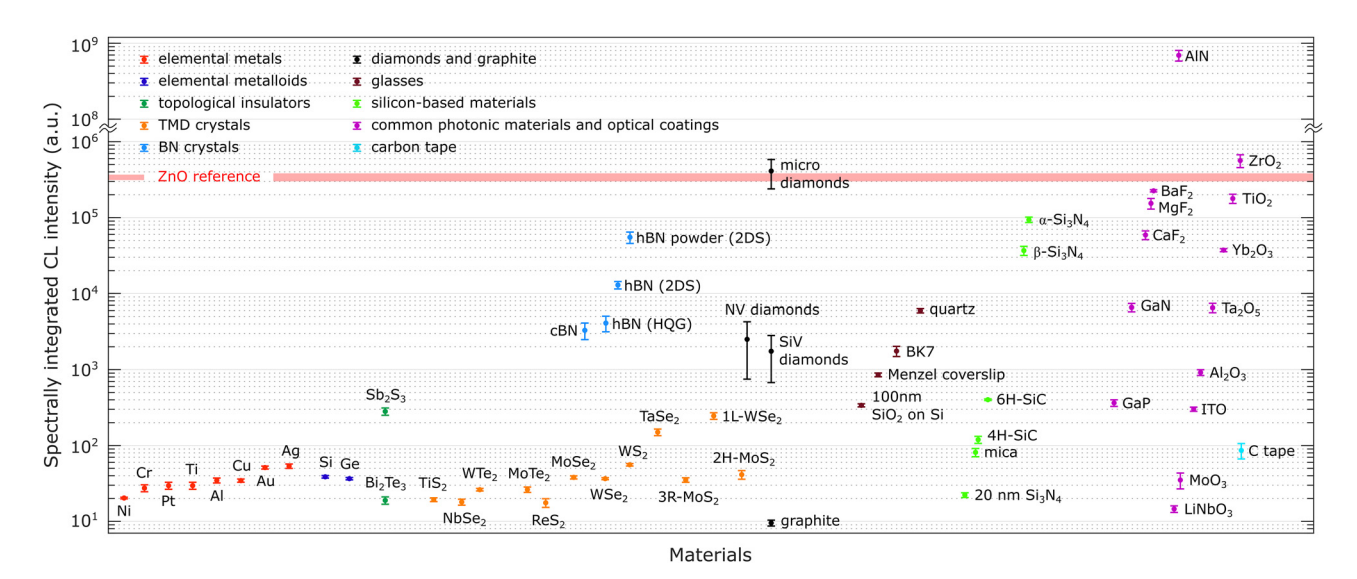


Figure 17: Comparison of CL intensity for investigated materials. Spectrally integrated CL intensity measured at ca. 1.4 nA and 10 keV. The error bar represents one standard deviation. The horizontal red-shaded area serves as a reference, representing the response of ZnO powder under identical acquisition and electron beam parameters.

current and a super-linear dependence on energy (Table 1). At higher acceleration voltages, the intensity of indirect bandgap emission saturates, a trend previously observed in doped GaP samples [178].

In summary, the CL intensity of transition radiation shows a clear linear dependence on both electron beam current and energy. This behavior occurs because transition radiation is a coherent process that scales directly with the number of electrons (beam current) and their energy, as higher-energy electrons generate more photons by more effectively perturbing the electromagnetic field at the material interface. Similarly, excitonic emission intensity increases linearly with current, as a higher beam current provides more electrons to excite the sample. However, as electron beam energy increases, excitonic emission intensity in thin heterostructures decreases due to reduced excitation efficiency. At higher energies, electrons pass through the thin sample with minimal interaction, reducing the excitation efficiency of the hBN-encapsulated monolayer. In contrast, the CL intensity of bandgap- and defect-related emission exhibits a super-linear increase with electron beam energy, likely due to enhanced excitation efficiency. Higher-energy electrons penetrate deeper into the material, exciting a larger volume and potentially generating additional photons through secondary processes. However, the increased penetration depth could lead to self-absorption effects, resulting in a saturation of the intensity trend.

Finally, we report the spectrally integrated CL intensity for a wide selection of materials under identical electron beam parameters of 1.4 nA and 10 kV. Each material was measured at five different points on the sample, with

the setup realigned from scratch each time, allowing us to determine the mean CL intensity and its standard deviation, shown as error bars in Figure 17. As a reference, we used a ZnO powder, which commonly employed for alignment and calibration of CL systems, with its intensity indicated as a red-shaded area in Figure 17. Additionally, we report CL intensity for typical carbon tape used in CL microscopy. Reliable CL intensity values could not be obtained for polymeric and resist materials due to the specific CL measurement procedure and their rapid degradation under electron beam exposure.

7 Conclusions

This work presents a comprehensive atlas of CL response for a broad range of materials relevant to photonic and plasmonic applications. Through Monte Carlo simulations, we demonstrate how variations in electron beam energy and material density affect electron penetration and energy deposition profiles. By systematically characterizing materials under electron beam excitation across a range of energies, we provide detailed insights into the origins of coherent and incoherent CL. Our results highlight the distinct CL properties of metals, metalloids, topological insulators, TMDs, boron nitride, carbon-based materials, commonly used photonic materials and optical coatings, and polymers. Our findings aid in the selection of materials and substrates for advanced photonic and plasmonic experiments in an electron microscope. Additionally, this atlas serves as a foundational resource for future CL studies, offering

guidance on experimental parameters for optimal material characterization. This resource ultimately paves the way for novel applications in photonics and plasmonics, fostering innovative research in these fields.

Acknowledgments: We thank Dr. Catarina Ferreira for her comments and suggestions during the revision of the manuscript.

Research funding: The Center for Polariton-driven Light-Matter Interactions (POLIMA) is sponsored by the Danish National Research Foundation (Project No. DNRF165).

Author contributions: The idea of an atlas was conceived by SE and SM, who, along with YL and TY, contributed to the sample preparations. Cathodoluminescence spectroscopy was carried out by SE and SM, while YL and TY performed Raman spectroscopy. The project was supervised by SM and NAM. All authors contributed to analyzing the data and writing the manuscript. All authors have accepted responsibility for the entire content of this manuscript and consented to its submission to the journal, reviewed all the results and approved the final version of the manuscript.

Conflict of interest: Authors state no conflicts of interest. Data availability: The datasets generated and/or analyzed during the current study are available from the corresponding author upon reasonable request.

References

- [1] B. G. Yacobi and D. B. Holt, "Cathodoluminescence scanning electron microscopy of semiconductors," J. Appl. Phys., vol. 59, no. 4, pp. R1-R24, 1986.
- [2] T. Coenen, S. V. den Hoedt, and A. Polman, "A new cathodoluminescence system for nanoscale optics, materials science, and geology," Micros. Today, vol. 24, no. 3, pp. 12-19,
- [3] T. Coenen and N. M. Haegel, "Cathodoluminescence for the 21st century: learning more from light," Appl. Phys. Rev., vol. 4, no. 3, p. 031103, 2017.
- [4] J. Christopher, M. Taleb, A. Maity, M. Hentschel, H. Giessen, and N. Talebi, "Electron-driven photon sources for correlative electron-photon spectroscopy with electron microscopes," Nanophotonics, vol. 9, no. 15, pp. 4381-4406, 2020.
- [5] C. Roques-Carmes, et al., "Free-electron—light interactions in nanophotonics," Appl. Phys. Rev., vol. 10, no. 1, p. 011303,
- [6] F. J. García de Abajo, "Optical excitations in electron microscopy," Rev. Mod. Phys., vol. 82, no. 1, pp. 209-275, 2010.
- [7] F. J. García de Abajo and V. Di Giulio, "Optical excitations with electron beams: challenges and opportunities," ACS Photonics, vol. 8, no. 4, pp. 945-974, 2021.
- [8] L. J. Brillson, "Applications of depth-resolved cathodoluminescence spectroscopy," J. Phys. D: Appl. Phys., vol. 45, no. 18, p. 183001, 2012.

- [9] M. Kociak and L. F. Zagonel, "Cathodoluminescence in the scanning transmission electron microscope," Ultramicroscopy, vol. 176, pp. 112-131, 2017.
- [10] S. Meuret, et al., "Complementary cathodoluminescence lifetime imaging configurations in a scanning electron microscope," *Ultramicroscopy*, vol. 197, pp. 28 – 38, 2019.
- [11] M. Yoshikawa, Advanced Optical Spectroscopy Techniques for Semiconductors: Raman, Infrared, and Cathodoluminescence Spectroscopy, Cham, Switzerland, Springer International Publishing, 2023.
- [12] Z. Dang, Y. Chen, and Z. Fang, "Cathodoluminescence nanoscopy: state of the art and beyond," ACS Nano, vol. 17, no. 24, pp. 24431-24448, 2023.
- [13] B. G. Yacobi and D. B. Holt, Cathodoluminescence Microscopy of Inorganic Solids, New York, USA, Springer US, 1990.
- [14] H. Guthrey and J. Moseley, "A review and perspective on cathodoluminescence analysis of halide perovskites," Adv. Energy Mater., vol. 10, no. 26, p. 1903840, 2020.
- [15] A. Polman, M. Kociak, and F. J. García de Abajo, "Electron-beam spectroscopy for nanophotonics," Nat. Mater., vol. 18, no. 11, pp. 1158 – 1171, 2019.
- [16] R. Gómez-Medina, N. Yamamoto, M. Nakano, and F. J. García de Abajo, "Mapping plasmons in nanoantennas via cathodoluminescence," New J. Phys., vol. 10, no. 10, p. 105009, 2008.
- [17] T. Coenen, E. J. R. Vesseur, and A. Polman, "Angle-resolved cathodoluminescence spectroscopy," Appl. Phys. Lett., vol. 99, no. 14, p. 143103, 2011.
- [18] B. J. M. Brenny, T. Coenen, and A. Polman, "Quantifying coherent and incoherent cathodoluminescence in semiconductors and metals," J. Appl. Phys., vol. 115, no. 24, p. 244307, 2014.
- [19] S. Mignuzzi, et al., "Energy momentum cathodoluminescence spectroscopy of dielectric nanostructures," ACS Photonics, vol. 5, no. 4, pp. 1381-1387, 2018.
- [20] M. Scheucher, T. Schachinger, T. Spielauer, M. Stöger-Pollach, and P. Haslinger, "Discrimination of coherent and incoherent cathodoluminescence using temporal photon correlations," Ultramicroscopy, vol. 241, p. 113594, 2022.
- [21] S. Fiedler, et al., "Disentangling cathodoluminescence spectra in nanophotonics: particle eigenmodes vs transition radiation," Nano Lett., vol. 22, no. 6, pp. 2320-2327, 2022.
- [22] S. Yanagimoto, N. Yamamoto, T. Yuge, T. Sannomiya, and K. Akiba, "Unveiling the nature of cathodoluminescence from photon statistics," Commun. Phys., vol. 8, no. 56, 2025, https://doi .org/10.1038/s42005-025-01978-6.
- [23] D. Drouin, A. R. Couture, D. Joly, X. Tastet, V. Aimez, and R. Gauvin, "CASINO V2.42 — a fast and easy-to-use modeling tool for scanning electron microscopy and microanalysis users," Scanning, vol. 29, no. 3, pp. 92-101, 2007.
- [24] C. B. Norris, C. E. Barnes, and W. Beezhold, "Depth-resolved cathodoluminescence in undamaged and ion-implanted GaAs, ZnS, and CdS," J. Appl. Phys., vol. 44, no. 7, pp. 3209 – 3221, 1973.
- [25] L. H. G. Tizei and M. Kociak, "Spatially resolved quantum nano-optics of single photons using an electron microscope," Phys. Rev. Lett., vol. 110, no. 15, p. 153604, 2013.
- [26] L. Francaviglia, et al., "Optimizing cathodoluminescence microscopy of buried interfaces through nanoscale heterostructure design," Nanoscale, vol. 14, no. 20, pp. 7569 – 7578, 2022.

- [27] P. Hovington, D. Drouin, R. Gauvin, D. C. Joy, and N. Evans, "CASINO: a new Monte Carlo code in C language for electron beam interactions - part III: stopping power at low energies," Scanning, vol. 19, no. 1, pp. 29-35, 1997.
- [28] P. Hovington, D. Drouin, and R. Gauvin, "Casino: CASINO: a new Monte Carlo code in C language for electron beam interactions part I: description of the program," Scanning, vol. 19, no. 1, pp. 1-14, 1997.
- [29] D. Drouin, P. Hovington, and R. Gauvin, "Casino: CASINO: a new Monte Carlo code in C language for electron beam interactions - part II: tabulated values of the Mott cross section," Scanning, vol. 19, no. 1, pp. 20-28, 1997.
- [30] D. C. Joy and S. Luo, "An empirical stopping power relationship for low-energy electrons," *Scanning*, vol. 11, no. 4, pp. 176–180, 1989.
- [31] L. Reimer, Scanning Electron Microscopy: Physics of Image Formation and Microanalysis, Berlin, Germany, Springer Berlin Heidelberg,
- [32] R. F. Egerton, Electron Energy-Loss Spectroscopy in the Electron Microscope, New York, USA, Springer US, 2011.
- [33] K. Kanaya and S. Okayama, "Penetration and energy-loss theory of electrons in solid targets," J. Phys. D: Appl. Phys., vol. 5, no. 1, pp. 43-58, 1972.
- [34] L. Reimer and H. Drescher, "Secondary electron emission of 10-100 kev electrons from transparent films of Al and Au," J. Phys. D: Appl. Phys., vol. 10, no. 5, pp. 805-815, 1977.
- [35] E. H. Darlington and V. E. Cosslett, "Backscattering of 0.5-10 keV electrons from solid targets," J. Phys. D: Appl. Phys., vol. 5, no. 11, pp. 1969 – 1981, 1972.
- [36] S. Fiedler, et al., "Sub-to-super-Poissonian photon statistics in cathodoluminescence of color center ensembles in isolated diamond crystals," Nanophotonics, vol. 12, no. 12, pp. 2231-2237,
- [37] A. Tselin, et al., "Exploring the dielectric function of platinum," Phys. Rev. B. vol. 110, no. 19, p. 195130, 2024.
- [38] K. J. Palm, J. B. Murray, T. C. Narayan, and J. N. Munday, "Dynamic optical properties of metal hydrides," ACS Photonics, vol. 5, no. 11, pp. 4677-4686, 2018.
- [39] R. L. Olmon, et al., "Optical dielectric function of gold," Phys. Rev. B, vol. 86, no. 23, p. 235147, 2012.
- [40] P. Goldsmith and J. V. Jelley, "Optical transition radiation from protons entering metal surfaces," Philos. Mag., vol. 4, no. 43, pp. 836 – 844, 1959.
- [41] L. S. Cram and E. T. Arakawa, "Bremsstrahlung and transition radiation from Ag foils bombarded by non-normal incidence electrons," Phys. Rev., vol. 153, no. 2, pp. 455-459, 1967.
- [42] L. Wartski, S. Roland, J. Lasalle, M. Bolore, and G. Filippi, "Interference phenomenon in optical transition radiation and its application to particle beam diagnostics and multiple-scattering measurements," J. Appl. Phys., vol. 46, no. 8, pp. 3644-3653, 1975.
- [43] B. G. Papanicolaou, J. M. Chen, and C. A. Papageorgopoulos, "Cathodoluminescence of copper and nickel surfaces," J. Phys. Chem. Solids, vol. 37, no. 4, pp. 403-409, 1976.
- [44] L. Brillson, H. Richter, M. Slade, B. Weinstein, and Y. Shapira, "Cathodoluminescence spectroscopy studies of laser-annealed metal-semiconductor interfaces," J. Vac. Sci. Technol. A, vol. 3, no. 3, pp. 1011-1015, 1985.
- [45] L. J. Brillson, R. E. Viturro, J. L. Shaw, and H. W. Richter, "Cathodoluminescence spectroscopy of metal—semiconductor

- interface structures," J. Vac. Sci. Technol. A, vol. 6, no. 3, pp. 1437-1445, 1988.
- [46] R. E. Viturro, et al., "Arsenic- and metal-induced GaAs interface states by low-energy cathodoluminescence spectroscopy," J. Vac. Sci. Technol. B, vol. 6, no. 4, pp. 1397-1402, 1988.
- [47] M. V. Bashevoy, F. Jonsson, A. V. Krasavin, N. I. Zheludev, Y. Chen, and M. I. Stockman, "Generation of traveling surface plasmon waves by free-electron impact," Nano Lett., vol. 6, no. 6, pp. 1113-1115, 2006.
- [48] N. Yamamoto, K. Araya, and F. J. García de Abajo, "Photon emission from silver particles induced by a high-energy electron beam," Phys. Rev. B, vol. 64, no. 20, p. 205419, 2001.
- [49] R. A. Ferrell, "Predicted radiation of plasma oscillations in metal films," Phys. Rev., vol. 111, no. 5, pp. 1214-1222, 1958.
- [50] J. T. van Wijngaarden, E. Verhagen, A. Polman, C. E. Ross, H. J. Lezec, and H. A. Atwater, "Direct imaging of propagation and damping of near-resonance surface plasmon polaritons using cathodoluminescence spectroscopy," Appl. Phys. Lett., vol. 88, no. 22, p. 221111, 2006.
- [51] N. Yamamoto, M. Nakano, and T. Suzuki, "Light emission by surface plasmons on nanostructures of metal surfaces induced by high-energy electron beams," Surf. Interface Anal., vol. 38, nos. 12-13, pp. 1725-1730, 2006.
- [52] E. J. R. Vesseur, R. de Waele, M. Kuttge, and A. Polman, "Direct observation of plasmonic modes in Au nanowires using high-resolution cathodoluminescence spectroscopy," Nano Lett., vol. 7, no. 9, pp. 2843-2846, 2007.
- [53] N. Yamamoto, "Cathodoluminescence of surface plasmon induced light emission," in The Transmission Electron Microscope, chapter 15, K. Maaz, Ed., Rijeka, IntechOpen, 2012.
- [54] M. W. Knight, et al., "Aluminum plasmonic nanoantennas," Nano Lett., vol. 12, no. 11, pp. 6000 – 6004, 2012.
- [55] T. Coenen, F. B. Arango, A. F. Koenderink, and A. Polman, "Directional emission from a single plasmonic scatterer," Nat. Commun., vol. 5, p. 3250, 2014.
- [56] F.-P. Schmidt, A. Losquin, M. Horák, U. Hohenester, M. Stöger-Pollach, and J. R. Krenn, "Fundamental limit of plasmonic cathodoluminescence," Nano Lett., vol. 21, no. 1, pp. 590 – 596,
- [57] C. Chi, et al., "Selectively steering photon spin angular momentum via electron-induced optical spin Hall effect," Sci. Adv., vol. 7, no. 18, p. eabf8011, 2021.
- [58] D. T. Vu, N. Matthaiakakis, and T. Sannomiya, "Plasmonic nanopyramid array enhancing luminescence of MoS₂ investigated by cathodoluminescence," Adv. Opt. Mater., vol. 11, no. 20, 2023, https://doi.org/10.1002/adom.202300598.
- [59] E. Akerboom, V. Di Giulio, N. J. Schilder, F. J. García de Abajo, and A. Polman, "Free electron – plasmon coupling strength and near-field retrieval through electron energy-dependent cathodoluminescence spectroscopy," ACS Nano, vol. 18, no. 21, pp. 13560-13567, 2024.
- [60] M. Kociak and O. Stéphan, "Mapping plasmons at the nanometer scale in an electron microscope," Chem. Soc. Rev., vol. 43, no. 11, p. 3865, 2014.
- [61] A. Losquin, et al., "Unveiling nanometer scale extinction and scattering phenomena through combined electron energy loss spectroscopy and cathodoluminescence measurements," Nano Lett., vol. 15, no. 2, pp. 1229-1237, 2015.

- [62] J. K. Day, N. Large, P. Nordlander, and N. J. Halas, "Standing wave plasmon modes interact in an antenna-coupled nanowire," Nano Lett., vol. 15, no. 2, pp. 1324-1330, 2015.
- [63] K. Singh, et al., "Cathodoluminescence as a probe of the optical properties of resonant apertures in a metallic film," Beilstein J. Nanotechnol., vol. 9, pp. 1491-1500, 2018.
- [64] P. H. Bittorf, F. Davoodi, M. Taleb, and N. Talebi, "Mapping optical Bloch modes of a plasmonic square lattice in real and reciprocal spaces using cathodoluminescence spectroscopy," Opt. Express, vol. 29, no. 21, p. 34328, 2021.
- [65] R. Lingstädt, et al., "Electron beam induced circularly polarized light emission of chiral gold nanohelices," ACS Nano, vol. 17, no. 24, pp. 25496-25506, 2023.
- [66] N. Yamamoto, H. Sugiyama, and A. Toda, "Cherenkov and transition radiation from thin plate crystals detected in the transmission electron microscope," Proc. R. Soc. A, vol. 452, no. 1953, pp. 2279-2301, 1996.
- [67] M. A. Piestrup, et al., "Generation of hard x rays from transition radiation using high-density foils and moderate-energy electrons," Phys. Rev. A, vol. 43, no. 5, pp. 2387-2396, 1991.
- [68] J. Chen, et al., "Low-velocity-favored transition radiation," Phys. Rev. Lett., vol. 131, no. 11, p. 113002, 2023.
- [69] P. Borziak, I. Konovalov, Y. Kulyupin, and K. Pilipchak, "Cathodoluminescence from metal films," Thin Solid Films, vol. 35, no. 2, pp. L9-L12, 1976.
- [70] S. Myhajlenko, W. Ke, and B. Hamilton, "Cathodoluminescence assessment of electron beam recrystallized silicon," J. Appl. Phys., vol. 54, no. 2, pp. 862-867, 1983.
- [71] X.-L. Qi and S.-C. Zhang, "Topological insulators and superconductors," Rev. Mod. Phys., vol. 83, no. 4, pp. 1057-1110,
- [72] J.-Y. Ou, J.-K. So, G. Adamo, A. Sulaev, L. Wang, and N. I. Zheludev, "Ultraviolet and visible range plasmonics of a topological insulator," Nat. Commun., vol. 5, p. 5139, 2014.
- [73] R. Lingstädt, et al., "Interaction of edge exciton polaritons with engineered defects in the hyperbolic material Bi₂Se₃," Commun. Mater., vol. 2, no. 5, 2021, https://doi.org/10.1038/s43246-020-
- [74] Q. Yan, S. Wang, K. Guan, X. Guan, and L. He, "Cathodoluminescence and tip-plasmon resonance of Bi₂Te₃ triangular nanostructures," PLoS One, vol. 19, no. 1, p. e0291251, 2024.
- [75] I. Mediavilla-Martinez, et al., "Temperature dependence of the Raman spectrum of orthorhombic Bi₂Se₃," *arXiv:2402.07256*.
- [76] M. Zhong, et al., "High-performance photodetectors based on Sb₂S₃ nanowires: wavelength dependence and wide temperature range utilization," Nanoscale, vol. 9, no. 34, pp. 12364-12371, 2017.
- [77] S. Zheng, J.-K. So, F. Liu, Z. Liu, N. Zheludev, and H. J. Fan, "Giant enhancement of cathodoluminescence of monolayer transitional metal dichalcogenides semiconductors," Nano Lett., vol. 17, no. 10, pp. 6475-6480, 2017.
- [78] G. Nayak, et al., "Cathodoluminescence enhancement and quenching in type-I van der Waals heterostructures: cleanliness of the interfaces and defect creation," Phys. Rev. Mater., vol. 3, no. 11, p. 114001, 2019.
- [79] N. Bonnet, et al., "Nanoscale modification of WS₂ trion emission by its local electromagnetic environment," Nano Lett., vol. 21, no. 24, pp. 10178-10185, 2021.

- [80] S. Fiedler, et al., "Photon superbunching in cathodoluminescence of excitons in WS₂ monolayer," 2D Mater., vol. 10, no. 2, p. 021002,
- [81] M. T. A. Borghi and N. R. Wilson, "Cathodoluminescence from interlayer excitons in a 2D semiconductor heterobilayer," Nanotechnology, vol. 35, no. 46, p. 465203, 2024.
- [82] H. Sun, et al., "Unveiling sulfur vacancy pairs as bright and stable color centers in monolayer WS₂," Nat. Commun., vol. 15, p. 9476,
- [83] M. Taleb, F. Davoodi, F. K. Diekmann, K. Rossnagel, and N. Talebi, "Charting the exciton – polariton landscape of WSe₂ thin flakes by cathodoluminescence spectroscopy," Adv. Photonics Res., vol. 3, no. 1, p. 2100124, 2021.
- [84] F. Chahshouri, M. Taleb, F. K. Diekmann, K. Rossnagel, and N. Talebi, "Interaction of excitons with Cherenkov radiation in WSe₂ beyond the non-recoil approximation," J. Phys. D: Appl. Phys., vol. 55, no. 14, p. 145101, 2022.
- [85] D. T. Vu, N. Matthaiakakis, H. Saito, and T. Sannomiya, "Exciton-dielectric mode coupling in MoS₂ nanoflakes visualized by cathodoluminescence," Nanophotonics, vol. 11, no. 9, pp. 2129-2137, 2022.
- [86] S. Y. Woo and L. H. G. Tizei, "Nano-optics of transition metal dichalcogenides and their van der Waals heterostructures with electron spectroscopies," 2D Mater., vol. 12, no. 1, p. 012001,
- [87] B. Munkhbat, P. Wróbel, T. J. Antosiewicz, and T. O. Shegai, "Optical constants of several multilayer transition metal dichalcogenides measured by spectroscopic ellipsometry in the 300-1700 nm range: high index, anisotropy, and hyperbolicity," ACS Photonics, vol. 9, no. 7, pp. 2398-2407, 2022.
- [88] M. Negri, et al., "Excitonic absorption and defect-related emission in three-dimensional MoS₂ pyramids," Nanoscale, vol. 14, no. 4, pp. 1179-1186, 2022.
- [89] M. Mahajan, S. Kallatt, M. Dandu, N. Sharma, S. Gupta, and K. Majumdar, "Light emission from the layered metal 2H-TaSe, and its potential applications," Commun. Phys., vol. 2, no. 88, 2019, https://doi.org/10.1038/s42005-019-0190-0.
- [90] B. V. Shipilo, A. M. Zaitsev, E. M. Shishonok, and A. A. Mel'nikov, "Effect of annealing on cathodoluminescence of cubic boron nitride," J. Appl. Spectrosc., vol. 45, no. 4, pp. 1060-1063, 1986.
- [91] M. G. Silly, et al., "Luminescence properties of hexagonal boron nitride: cathodoluminescence and photoluminescence spectroscopy measurements," Phys. Rev. B, vol. 75, no. 8, p. 085205, 2007.
- [92] R. Bourrellier, et al., "Bright UV single photon emission at point defects in h-BN," Nano Lett., vol. 16, no. 7, pp. 4317 – 4321, 2016.
- [93] A. Tararan, et al., "Optical gap and optically active intragap defects in cubic BN," Phys. Rev. B, vol. 98, no. 9, p. 094106, 2018.
- [94] B. Shevitski, et al., "Blue-light-emitting color centers in high-quality hexagonal boron nitride," Phys. Rev. B, vol. 100, no. 15, p. 155419, 2019.
- [95] F. Hayee, et al., "Revealing multiple classes of stable quantum emitters in hexagonal boron nitride with correlated optical and electron microscopy," Nat. Mater., vol. 19, no. 5, pp. 534-539,
- [96] R. J. P. Roman, et al., "Band gap measurements of monolayer h-BN and insights into carbon-related point defects," 2D Mater., vol. 8, no. 4, p. 044001, 2021.

- [97] A. Gale, et al., "Site-specific fabrication of blue quantum emitters in hexagonal boron nitride," ACS Photonics, vol. 9, no. 6, pp. 2170 – 2177, 2022.
- [98] S. Roux, et al., "Cathodoluminescence monitoring of quantum emitter activation in hexagonal boron nitride," Appl. Phys. Lett., vol. 121, no. 18, p. 184002, 2022.
- [99] F. Bianco, E. Corte, S. D. Tchernij, J. Forneris, and F. Fabbri, "Engineering multicolor radiative centers in hBN flakes by varying the electron beam irradiation parameters," Nanomaterials, vol. 13, no. 4, p. 739, 2023.
- [100] C. A. Taylor, S. W. Brown, V. Subramaniam, S. Kidner, S. C. Rand, and R. Clarke, "Observation of near-band-gap luminescence from boron nitride films," Appl. Phys. Lett., vol. 65, no. 10, pp. 1251-1253, 1994.
- [101] W. J. Zhang, H. Kanda, and S. Matsumoto, "Cathodoluminescence of cubic boron nitride films deposited by chemical vapor deposition," Appl. Phys. Lett., vol. 81, no. 18, pp. 3356-3358, 2002.
- [102] K. Watanabe, T. Taniguchi, and H. Kanda, "Direct-bandgap properties and evidence for ultraviolet lasing of hexagonal boron nitride single crystal," Nat. Mater., vol. 3, no. 6, pp. 404-409,
- [103] L. Schué, et al., "Dimensionality effects on the luminescence properties of hBN," Nanoscale, vol. 8, no. 13, pp. 6986-6993,
- [104] M. Bogroff, et al., "Non-perturbative cathodoluminescence microscopy of beam-sensitive materials," Nanophotonics, vol. 14, no. 11, pp. 2095 - 2101, 2025.
- [105] A. Ganyecz, R. Babar, Z. Benedek, I. Aharonovich, G. Barcza, and V. Ivády, "First-principles theory of the nitrogen interstitial in hBN: a plausible model for the blue emitter," Nanoscale, vol. 16, no. 8, pp. 4125-4139, 2024.
- [106] A. M. Zaitsev, Optical Properties of Diamond, Berlin Heidelberg, Springer, 2001.
- [107] E. H. L. Falcao and F. Wudl, "Carbon allotropes: beyond graphite and diamond," J. Chem. Technol. Biotechnol., vol. 82, no. 6, pp. 524-531, 2007.
- [108] G. S. Woods and A. R. Lang, "Cathodoluminescence, optical absorption and x-ray topographic studies of synthetic diamonds," *I. Cryst. Growth*, vol. 28, no. 2, pp. 215 – 226, 1975.
- [109] C. Bradac, W. Gao, J. Forneris, M. E. Trusheim, and I. Aharonovich, "Quantum nanophotonics with group IV defects in diamond," Nat. Commun., vol. 10, p. 5625, 2019.
- [110] S. Meuret, et al., "Photon bunching in cathodoluminescence," Phys. Rev. Lett., vol. 114, no. 19, p. 197401, 2015.
- [111] V. Iyer, K. Roccapriore, J. Ng, B. Srijanto, D. Lingerfelt, and B. Lawrie, "Photon bunching in cathodoluminescence induced by indirect electron excitation," Nanoscale, vol. 15, no. 22, pp. 9738-9744, 2023.
- [112] I. Kostova, L. Tormo, E. Crespo-Feo, and J. Garcia-Guinea, "Study of coal and graphite specimens by means of Raman and cathodoluminescence," Spectrochim. Acta A Mol. Biomol. Spectrosc., vol. 91, pp. 67-74, 2012.
- [113] J. Garcia-Guinea, V. Correcher, N. Can, F. Garrido, and P. D. Townsend, "Cathodoluminescence spectra recorded from surfaces of solids with hydrous molecules," J. Electron Spectrosc. Relat. Phenom., vol. 227, pp. 1-8, 2018.
- [114] V. S. Sedov, et al., "Color centers in silic on-doped diamond films," J. Appl. Spectrosc., vol. 83, no. 2, pp. 229-233, 2016.

- [115] J. N. Becker and E. Neu, "The silicon vacancy center in diamond," Semiconduct. Semimet., vol. 103, pp. 201-235, 2020.
- [116] H. Koyama, "Cathodoluminescence study of SiO₂," J. Appl. Phys., vol. 51, no. 4, pp. 2228-2235, 1980.
- [117] J. P. Mitchell and D. G. Denure, "A study of SiO layers on Si using cathodoluminescence spectra," Solid-State Electron., vol. 16, no. 7, pp. 825-839, 1973.
- [118] H. Koyama, K. Matsubara, and M. Mouri, "Cathodoluminescence study of a silicon dioxide layer on silicon with the aid of Auger electron spectroscopy," J. Appl. Phys., vol. 48, no. 12, pp. 5380 - 5381, 1977.
- [119] L. N. Skuja and W. Entzian, "Cathodoluminescence of intrinsic defects in glassy SiO₂, thermal SiO₂ films, and α -quartz," *Phys.* Status Solidi A, vol. 96, no. 1, pp. 191-198, 1986.
- [120] M. A. Stevens Kalceff and M. R. Phillips, "Cathodoluminescence microcharacterization of the defect structure of quartz," Phys. Rev. B, vol. 52, no. 5, pp. 3122-3134, 1995.
- [121] H.-J. Fitting, et al., "Cathodoluminescence of wet, dry, and hydrogen-implanted silica films," J. Non-Cryst. Solids, vol. 351, no. 27, pp. 2251-2262, 2005.
- [122] M. A. Stevens-Kalceff, "Cathodoluminescence microcharacterization of electron radiation induced defects in borosilicate glasses," Microsc. Microanal., vol. 14, no. S2, pp. 650-651, 2008.
- [123] A. Fali, et al., "Nanoscale spectroscopy of dielectric properties of mica," ACS Photonics, vol. 8, no. 1, pp. 175-181, 2020.
- [124] E. Sörman, N. T. Son, W. M. Chen, O. Kordina, C. Hallin, and E. Janzén, "Silicon vacancy related defect in 4H and 6H SiC," Phys. Rev. B, vol. 61, no. 4, pp. 2613-2620, 2000.
- [125] A. Kakanakova-Georgieva, R. Yakimova, A. Henry, M. K. Linnarsson, M. Syväjärvi, and E. Janzén, "Cathodoluminescence identification of donor – acceptor related emissions in as-grown 4H-SiC layers," *J. Appl. Phys.*, vol. 91, no. 5, pp. 2890-2895, 2002.
- [126] L. Ottaviani, P. Hidalgo, H. Idrissi, M. Lancin, S. Martinuzzi, and B. Pichaud, "Structural characterization of 6H-and 4H-SiC polytypes by means of cathodoluminescence and x-ray topography," J. Phys.: Condens. Matter, vol. 16, no. 2, p. S107, 2003.
- [127] S. Castelletto, et al., "Silicon carbide photonics bridging quantum technology," ACS Photonics, vol. 9, no. 5, pp. 1434-1457, 2022.
- [128] J. Q. Hu, Y. Bando, T. Sekiguchi, F. F. Xu, and J. H. Zhan, "Two-dimensional extremely thin single-crystalline α -Si₃N₄ microribbons," Appl. Phys. Lett., vol. 84, no. 5, pp. 804-806, 2004.
- [129] T. Sekiguchi, J. Hu, and Y. Bando, "Cathodoluminescence study of one-dimensional free-standing widegap-semiconductor nanostructures: GaN nanotubes, Si₃N₄ nanobelts and ZnS/Si nanowires," J. Electron Microsc., vol. 53, no. 2, pp. 203-208, 2004.
- [130] J. Huang, Z. Huang, S. Yi, Y. Liu, M. Fang, and S. Zhang, "Fe-catalyzed growth of one-dimensional α -Si $_3$ N $_4$ nanostructures and their cathodoluminescence properties," Sci. Rep., vol. 3, p. 3504, 2013.
- [131] W. Zhu, B. McEntire, Y. Enomoto, M. Boffelli, and G. Pezzotti, "Point-defect populations as induced by cation/anion substitution in β -Si₃N₄ lattice. A cathodoluminescence study," *J. Phys. Chem. C*, vol. 119, no. 6, pp. 3279-3287, 2015.
- [132] D. Maestre, A. Cremades, J. Piqueras, and L. Gregoratti, "Thermal growth and structural and optical characterization of indium tin oxide nanopyramids, nanoislands, and tubes," J. Appl. Phys., vol. 103, no. 9, p. 093531, 2008.

- [133] K.-Y. Pan, L.-D. Lin, L.-W. Chang, and H. C. Shih, "Studies on the optoelectronic properties of the thermally evaporated tin-doped indium oxide nanostructures," Appl. Surf. Sci., vol. 273, pp. 12-18,
- [134] S. Battiston, et al., "Cathodoluminescence evaluation of oxygen vacancy population in nanostructured titania thin films for photocatalytic applications," J. Phys. Chem. A, vol. 114, no. 16, pp. 5295-5298, 2010.
- [135] B. Santara, P. K. Giri, K. Imakita, and M. Fujii, "Evidence of oxygen vacancy induced room temperature ferromagnetism in solvothermally synthesized undoped TiO₂ nanoribbons," Nanoscale, vol. 5, no. 12, pp. 5476 – 5488, 2013.
- [136] M. Machreki, et al., "The role of lattice defects on the optical properties of TiO₂ nanotube arrays for synergistic water splitting," ACS Omega, vol. 8, no. 37, pp. 33255 – 33265, 2023.
- [137] M. Boffelli, et al., "Oxygen hole states in zirconia lattices: quantitative aspects of their cathodoluminescence emission," J. Phys. Chem. A, vol. 118, no. 42, pp. 9828-9836, 2014.
- [138] J.-H. Hur, S. Park, and U.-I. Chung, "First principles study of oxygen vacancy states in monoclinic ZrO₂: interpretation of conduction characteristics," J. Appl. Phys., vol. 112, no. 11, p. 113719, 2012.
- [139] A. P. Baraban, V. A. Dmitriev, V. E. Drozd, V. A. Prokofiev, S. N. Samarin, and E. O. Filatova, "Interface properties of Si-SiO₂-Ta₂O₅ structure by cathodoluminescence spectroscopy," J. Appl. Phys., vol. 119, no. 5, p. 055307, 2016.
- [140] J. Lee, W. D. Lu, and E. Kioupakis, "Electronic and optical properties of oxygen vacancies in amorphous Ta₂O₅ from first principles," *Nanoscale*, vol. 9, no. 3, pp. 1120-1127, 2017.
- [141] Y. Zhao, et al., "Preparation of MoO₃ nanostructures and their optical properties," J. Phys.: Condens. Matter, vol. 15, no. 35, pp. L547-L552, 2003.
- [142] K. Koike, R. Wada, S. Yaqi, Y. Harada, S. Sasa, and M. Yano, "Characteristics of MoO₃ films grown by molecular beam epitaxy," Jpn. J. Appl. Phys., vol. 53, no. 5S1, p. 05FJ02, 2014.
- [143] J. Llopis, C. Ballesteros, R. González, and Y. Chen, "Cathodoluminescence emission from LiNbO₃ single crystals," J. Appl. Phys., vol. 56, no. 2, pp. 460-462, 1984.
- [144] M. Ghamnia, C. Jardin, L. Martinez, M. Bouslama, and P. Durupt, "Electronic spectroscopy (AES, EELS) and cathodoluminescence (CL) for α -Al₂O₃ characterization," *Vacuum*, vol. 48, no. 2, pp. 129-134, 1997.
- [145] G. Demol, T. Paulmier, and D. Payan, "Cathodoluminescence of aluminum ceramic compounds," J. Appl. Phys., vol. 125, no. 2, p. 025110, 2019.
- [146] A. O. Dikovska, T. Okato, P. A. Atanasov, and M. Obara, "Cathodoluminscent properties of pulsed laser deposited Er, Yb co-doped Y₂O₃ thin films," J. Phys. D: Appl. Phys., vol. 37, no. 23, pp. L41-L44, 2004.
- [147] R. A. Buchanan, K. A. Wickersheim, J. J. Pearson, and G. F. Herrmann, "Energy levels of Yb3+ in gallium and aluminum garnets. I. Spectra," Phys. Rev., vol. 159, no. 2, pp. 245-251,
- [148] T. Mattila and R. M. Nieminen, "Ab initio study of oxygen point defects in GaAs, GaN, and AlN," Phys. Rev. B, vol. 54, no. 23, pp. 16676-16682, 1996.
- [149] S. O. Kucheyev, M. Toth, M. R. Phillips, J. S. Williams, and C. Jagadish, "Effects of excitation density on cathodoluminescence from GaN," Appl. Phys. Lett., vol. 79, no. 14, pp. 2154-2156, 2001.

- [150] H. Lei, H. S. Leipner, J. Schreiber, J. L. Weyher, T. Wosiński, and I. Grzegory, "Raman and cathodoluminescence study of dislocations in GaN," J. Appl. Phys., vol. 92, no. 11, pp. 6666-6670,
- [151] D. R. Wight, "Green luminescence efficiency in gallium phosphide," J. Phys. D: Appl. Phys., vol. 10, no. 4, pp. 431-454,
- [152] C. A. Dimitriadis, E. Huang, and S. M. Davidson, "SEM cathodoluminescence studies of dislocation recombination in GaP," Solid-State Electron., vol. 21, nos. 11-12, pp. 1419-1423,
- [153] M. A. Stevens-Kalceff, I. M. Tiginyanu, S. Langa, H. Föll, and H. L. Hartnagel, "Correlation between morphology and cathodoluminescence in porous GaP," J. Appl. Phys., vol. 89, no. 5, pp. 2560 - 2565, 2001.
- [154] M. Topaksu, V. Correcher, and J. Garcia-Guinea, "Luminescence emission of natural fluorite and synthetic CaF₂:Mn (TLD-400)," Radiat. Phys. Chem., vol. 119, pp. 151-156, 2016.
- [155] R. Rodríguez, V. Correcher, J. M. Gómez-Ros, J. L. Plaza, and J. Garcia-Guinea, "Cathodoluminescence, SEM and EDX analysis of CaF₂ and Tm₂O₃ pellets for radiation dosimetry applications," Radiat. Phys. Chem., vol. 188, p. 109621, 2021.
- [156] H. Yoshida, M. Hayashi, and M. Itoh, "Intensity enhancement of Auger-free luminescence in BaF₂ and CsCl by acceleration voltage of electron-beam excitation," Jpn. J. Appl. Phys., vol. 39, no. 3A, p. L215, 2000.
- [157] N. Li, C. P. Ho, S. Zhu, Y. H. Fu, Y. Zhu, and L. Y. T. Lee, "Aluminium nitride integrated photonics: a review," Nanophotonics, vol. 10, no. 9, pp. 2347-2387, 2021.
- [158] R. A. Youngman and J. H. Harris, "Luminescence studies of oxygen-related defects in aluminum nitride," J. Am. Ceram. Soc., vol. 73, no. 11, pp. 3238-3246, 1990.
- [159] P. J. Wellmann, U. Karl, S. Kleber, and H. Schmitt, "Cathodoluminescence characterization of organic semiconductor materials for light emitting device applications," J. Appl. Phys., vol. 101, no. 11, p. 113704, 2007.
- [160] C. G. Bischak, et al., "Cathodoluminescence-activated nanoimaging: noninvasive near-field optical microscopy in an electron microscope," Nano Lett., vol. 15, no. 5, pp. 3383 – 3390,
- [161] B. Qiao, G. Teyssedre, and C. Laurent, "Electroluminescence and cathodoluminescence from polyethylene and polypropylene films: spectra reconstruction from elementary components and underlying mechanisms," J. Appl. Phys., vol. 119, no. 2, p. 024103,
- [162] A. P. Tyutnev, V. S. Saenko, A. V. Vannikov, and G. S. Mingaleev, "Radiation-induced conductivity in polyethylene," Phys. Status Solidi A, vol. 78, no. 2, pp. 689-696, 1983.
- [163] C. A. Barrios, et al., "Fabrication of luminescent nanostructures by electron-beam direct writing of PMMA resist," Mater. Lett., vol. 88, pp. 93-96, 2012.
- [164] R. F. Egerton, "Radiation damage to organic and inorganic specimens in the tem," *Micron*, vol. 119, pp. 72–87, 2019.
- [165] L. Wang, et al., "One-dimensional electrical contact to a two-dimensional material," Science, vol. 342, no. 6158, pp. 614-617, 2013.
- [166] A. Castellanos-Gomez, et al., "Deterministic transfer of two-dimensional materials by all-dry viscoelastic stamping," 2D Mater., vol. 1, no. 1, p. 011002, 2014.

- [167] F. Yang, et al., "2D organic materials for optoelectronic applications," Adv. Mater., vol. 30, no. 2, p. 1702415, 2017.
- [168] A. E. Grigorescu and C. W. Hagen, "Resists for sub-20-nm electron beam lithography with a focus on HSQ: state of the art," Nanotechnology, vol. 20, no. 29, p. 292001, 2009.
- [169] D. Roitman, A. Karnieli, S. Tsesses, Z. Barkay, and A. Arie, "Coherent radiation at visible wavelengths from sub-keV electron beams," Opt. Lett., vol. 49, no. 8, p. 2013, 2024.
- [170] S. Y. Chou, P. R. Krauss, and P. J. Renstrom, "Nanoimprint lithography," J. Vac. Sci. Technol. B, vol. 14, no. 6, pp. 4129-4133, 1996.
- [171] M. Aktary, M. O. Jensen, K. L. Westra, M. J. Brett, and M. R. Freeman, "High-resolution pattern generation using the epoxy novolak SU-8 2000 resist by electron beam lithography," J. Vac. Sci. Technol. B, vol. 21, no. 4, pp. L5-L7, 2003.
- [172] D. B. Wittry and D. F. Kyser, "Measurement of diffusion lengths in direct-gap semiconductors by electron-beam excitation," J. Appl. Phys., vol. 38, no. 1, pp. 375-382, 1967.
- [173] J. Bok and P. Schauer, "Apparatus for temperature-dependent cathodoluminescence characterization of materials," Meas. Sci. Technol., vol. 25, no. 7, p. 075601, 2014.

- [174] T. S. Rao-Sahib and D. B. Wittry, "Measurement of diffusion lengths in p-type gallium arsenide by electron beam excitation," J. Appl. Phys., vol. 40, no. 9, pp. 3745-3750, 1969.
- [175] P. H. Bittorf, F. Majstorovic, P. Ruchka, H. Giessen, and N. Talebi, "A multi-dimensional cathodoluminescence detector with 3D printed micro-optics on a fiber," arXiv:2501.17723.
- [176] F. Koch, W. Hergert, G. Oelgart, and N. Puhlmann, "Determination of semiconductor parameters by electron beam induced current and cathodoluminescence measurements," Phys. Status Solidi A, vol. 109, no. 1, pp. 261-272, 1988.
- [177] S. Morozov, T. Yezekyan, C. Wolff, S. I. Bozhevolnyi, and N. A. Mortensen, "Inducing room-temperature valley polarization of excitonic emission in transition metal dichalcogenide monolayers," npj 2D Mater. Appl., vol. 8, no. 24, 2024, https://doi .org/10.1038/s41699-024-00459-8.
- [178] H. C. Casey and J. S. Jayson, "Cathodoluminescent measurements in GaP (Zn, O)," *J. Appl. Phys.*, vol. 42, no. 7, pp. 2774 – 2776, 1971.

Supplementary Material: This article contains supplementary material (https://doi.org/10.1515/nanoph-2025-0135).